Climate Impacts of Large-Scale Wind Farms as Parameterized in a Global Climate Model

ANNA C. FITCH*

National Center for Atmospheric Research, Boulder, Colorado

ABSTRACT

The local, regional, and global climate impacts of a large-scale global deployment of wind power in regionally high densities over land are investigated for a 60-yr period. Wind farms are represented as elevated momentum sinks as well as enhanced turbulence to represent turbine blade mixing in the Community Atmosphere Model, version 5 (CAM5), a global climate model. For a total installed capacity of 2.5 TW, to provide 16% of the world's projected electricity demand in 2050, minimal impacts are found both regionally and globally on temperature, sensible and latent heat fluxes, cloud, and precipitation. A mean near-surface warming of 0.12 ± 0.07 K is seen within the wind farms, with a global-mean temperature change of −0.013 ± 0.015 K. Impacts on wind speed and turbulence are more pronounced but largely confined within the wind farm areas. Increasing the wind farm areas to provide an installed capacity of 10 TW, or 65% of the 2050 electricity demand, causes further impacts; however, they remain slight overall. Maximum temperature changes are less than 0.5 K in the wind farm areas. To provide 20 TW of installed capacity, or 130% of the 2050 electricity demand, impacts both within the wind farms and beyond become more pronounced, with a doubling in turbine density. However, maximum temperature changes remain less than 0.7 K. Representing wind farms instead as an increase in surface roughness generally produces similar mean results; however, maximum changes increase, and influences on wind and turbulence are exaggerated. Overall, wind farm impacts are much weaker than those expected from greenhouse gas emissions, with very slight global-mean climate impacts.

1. Introduction

There has been much interest recently in the possibility of large deployments of wind power affecting weather and climate. With many wind farms in development on agricultural land, there are concerns related to, in particular, near-surface temperature and humidity changes. Wind power is one of the fastest-growing sources of energy, with installed capacity more than doubling from 121 GW in 2008 to 318 GW at the end of 2013 (Global Wind Energy Council 2014). Wind energy currently supplies 3% of the world's electricity demand, with targets to generate 15%–18% in 2050 (Philibert et al. 2013) with an installed capacity of 2.3–2.8 TW. This work

investigates the potential climate impacts of a large-scale global deployment of wind power in regionally high densities over land, with installed capacities to generate up to 130% of the world's projected electricity demand in 2050.

Enhanced turbulent mixing in the wake of wind farms has been shown to lead to a near-surface warming in stable (nocturnal) conditions and a cooling in unstable (daytime) conditions (e.g., Baidya Roy and Traiteur 2010). In a stable boundary layer, enhanced turbulent mixing in the wake causes mixing of higher potential-temperature (θ) air downward and, conversely, in an unstable boundary layer, lower θ air is mixed down. The changes in near-surface temperature may in turn affect sensible heat fluxes. Observations during one night in the wake of a large wind farm located on agricultural land showed little change in hub height temperatures; however, there was a near-surface warming of 1.0–1.5 K (Smith et al. 2013). Daytime temperature changes were very small. These results are consistent with those of Rajewski et al. (2013), who saw individual periods of near-surface warming of up to 1.5 K in the direct wake

* Current affiliation: Swedish Meteorological and Hydrological Institute, Norrköping, Sweden.

Corresponding author address: Anna C. Fitch, Swedish Meteorological and Hydrological Institute, 601 76 Norrköping, Sweden.
E-mail: anna.fitch@outlook.com

of a single row of turbines during nighttime. They found little impact on sensible heat fluxes. Zhou et al. (2012) examined satellite observations of temperature changes in a large wind farm and found small daytime temperature changes and a mean warming of up to 0.7 K at night for observations of one season over 9 years. These results contrasted with the previous study of Baidya Roy and Traiteur (2010), who found greater cooling of up to 2 K. In a wind tunnel study, Zhang et al. (2013) found the overall surface heat flux change was small within a model wind farm consisting of 12 rows of turbines. The mean surface heat flux was reduced by 4% when the turbines were staggered, and there was almost no change when the turbines were aligned.

With the paucity of observations, most investigations into the potential climate impacts of wind farms have taken the form of modeling studies. These studies have employed global climate models, using two main types of parameterization to represent the effects of wind farms. Earlier investigations represented large wind farms as an increase in the surface aerodynamic roughness length z_0 over wind farm areas (Ivanova and Nadyozhina 2000; Keith et al. 2004; Kirk-Davidoff and Keith 2008; Barrie and Kirk-Davidoff 2010; Wang and Prinn 2010, 2011). However, Fitch et al. (2013b) showed this method of parameterization to be insufficient in capturing the main characteristics of wind farm–induced flow produced by more sophisticated methods in mesoscale and large-eddy simulations (LES). In these models, wind farms are represented as elevated momentum sinks (in both mesoscale and LES models) and sources of turbulent kinetic energy (TKE) (in mesoscale models only) in model levels within the rotor area. The latter represents the mixing of the turbine blades. Jacobson and Archer (2012) also found deficiencies with a surface roughness parameterization in simulating wind speeds with a global model. Studies employing the enhanced z_0 method found near-surface temperature changes of 1–2 K over wind farm areas, contrasting with mesoscale and LES studies where mean temperature changes were less than 1 K (Baidya Roy et al. 2004; Baidya Roy and Traiteur 2010; Lu and Porté-Agel 2011; Fitch et al. 2013a). Surface heat fluxes were exaggerated with the enhanced z_0 method, leading to greater near-surface temperature changes.

More recent studies employing global models have represented wind farms as elevated momentum sinks, as in mesoscale studies, but without any treatment of turbine blade–generated turbulence. Marvel et al. (2013) found that uniformly distributed turbines across the globe would increase the zonal-mean temperature by approximately 0.1 K and decrease precipitation by around 1% for the present-day global energy demand. However, they did not study the potential climate impacts of high regional densities of wind turbines or for future energy demand scenarios. Jacobson and Archer (2012) found a surface cooling of more than 1 K in a global simulation of wind turbines located at the height of the jet stream. In a regional climate model simulation, Vautard et al. (2014) found a mean warming of 0.1 K over wind farm areas over a 33-yr period and a slight increase in precipitation of 0.01 mm day^{-1}. There was also a mean reduction in sensible heat flux of 1 W m^{-2} and an increase in latent heat flux of 0.4 W m^{-2}. Their study focused on 2020 targets for wind energy in Europe and did not look at other regions or possible interaction with the larger-scale flow.

The elevated momentum sink approach for representing wind farms extracts momentum in the layers of the atmosphere directly interacting with the turbine blades, whereas the enhanced z_0 method produces a momentum sink near the surface. The former allows the wind farm wake and associated surface impacts to be modeled by a combination of the resolved turbulent structures (in high-resolution mesoscale simulations and LES only) and the model physical parameterizations (in mesoscale and global models). The changes in near-surface meteorological conditions are thus simulated indirectly. Conversely, in the enhanced z_0 approach, the near-surface meteorological conditions are directly modified through the increased roughness length and are not a physical response to an elevated perturbation. In mesoscale and global models, bulk surface flux parameterizations are generally based on Monin–Obukhov similarity theory. In these parameterizations, larger z_0 represents a rougher surface that enhances mixing in the surface layer, in turn increasing the surface fluxes (discussed in section 2). In summary, changing z_0 over wind farm areas also directly modifies the surface fluxes, leading to changes in near-surface temperature.

We investigate the potential climate impacts of a large-scale global deployment of wind power in regionally high densities over land using a global climate model, the Community Atmosphere Model, version 5 (CAM5). Wind turbines are represented as an elevated momentum sink together with enhanced turbulence to represent turbine blade mixing. The resulting climate impacts are compared with the enhanced surface roughness approach used in previous studies. Although Fitch et al. (2013b) compared the two approaches, they did not investigate climate impacts, and idealized simulations were used without coupling to a land surface model.

The paper is organized as follows: Section 2 presents a brief description of the wind farm parameterization and its integration with CAM5, along with the configuration of the model simulations. Section 3 presents the results for impacts of wind farms on temperature, wind, TKE, cloud, precipitation, and surface heat fluxes. Section 4 concludes with a discussion.

2. Experimental method

a. Wind farm parameterization

To represent the influence of wind farms on the atmosphere, we incorporate the parameterization employed in Fitch et al. (2012, 2013a,b) into CAM5. The parameterization represents the drag force of wind turbines within model layers containing turbine blades. The force of drag is a function of wind speed and turbine rotor area, as well as the turbine density in the horizontal. It improves upon previous elevated momentum sink parameterizations in global models (Marvel et al. 2013; Jacobson and Archer 2012) by representing the total fraction of kinetic energy (KE) extracted from the atmosphere by wind turbines, as well as including treatment of turbine blade–generated turbulence. Heat release through electricity use was not included in the model as in Jacobson and Archer (2012) (who added heat to the lowest model level over the wind farm areas), as this would impact the temperature directly rather than allowing changes to evolve through turbine–atmosphere interactions alone. The equations applied in the model are reproduced below. For the full derivation the reader is referred to Fitch et al. (2012).

The horizontal momentum sink term in grid cell i, j, k, where i, j, and k correspond to the zonal, meridional, and vertical coordinates, respectively, is

$$\frac{\partial |\mathbf{V}|_{ijk}}{\partial t} = -\frac{\frac{1}{2} N_t^{ij} C_T |\mathbf{V}|_{ijk}^2 A_{ijk}}{(z_{k+1} - z_k)}, \quad (1)$$

where $\mathbf{V} = (u, v)$ is the horizontal wind velocity vector, N_t is the number of turbines per square meter, C_T is the velocity-dependent thrust coefficient of the turbine, and A_{ijk} is the cross-sectional rotor area of one wind turbine bounded by model levels k and $k + 1$. The term z_k represents the height above ground at model level k.

Expressing Eq. (1) in component form gives the horizontal momentum tendency terms applied in the model:

$$\frac{\partial u_{ijk}}{\partial t} = \frac{u_{ijk}}{|\mathbf{V}|_{ijk}} \frac{\partial |\mathbf{V}|_{ijk}}{\partial t} \quad \text{and} \quad (2)$$

$$\frac{\partial v_{ijk}}{\partial t} = \frac{v_{ijk}}{|\mathbf{V}|_{ijk}} \frac{\partial |\mathbf{V}|_{ijk}}{\partial t}. \quad (3)$$

The thrust coefficient C_T quantifies the total fraction of KE extracted from the flow through the rotor area. It is particular to each type of turbine and is a function of wind speed. A fraction of this KE is converted into electrical energy, represented by the power coefficient C_P and is also a function of wind speed. For the turbines modeled here, C_P varies between 17% and 75% of C_T. Previous studies have quantified the total fraction of KE

extracted from the flow by C_P; thus, in this case, the drag may be underestimated by up to a factor of nearly 6. The C_T and C_P coefficients are measured by turbine manufacturers. The fraction of KE extracted by the turbines that does not produce electrical energy (i.e., the nonproductive drag) produces TKE, assuming mechanical and electrical losses are relatively small. The fraction of energy converted into TKE is given by $C_{\text{TKE}} = C_T - C_P$, and the source of TKE applied in the model is

$$\frac{\partial \text{TKE}_{ijk}}{\partial t} = \frac{\frac{1}{2} N_t^{ij} C_{\text{TKE}} |\mathbf{V}|_{ijk}^3 A_{ijk}}{(z_{k+1} - z_k)}. \quad (4)$$

The additional TKE allows enhanced vertical mixing in the model. However, it does not reproduce detailed finescale turbulent motions as seen from observations or LES, as the diffusion is uniform within a grid cell.

b. Coupling with planetary boundary layer physics

The wind farm parameterization is coupled with the University of Washington Moist Turbulence (UWMT) parameterization (Bretherton and Park 2009) in CAM5. UWMT uses a first-order turbulence closure (Mellor and Yamada 1982) based on moist conserved variables. All turbulence is represented using downgradient diffusion of turbulent fluxes of the form

$$\overline{w'\chi'} = -K_\chi \frac{\partial \chi}{\partial z}. \quad (5)$$

The eddy diffusivities for momentum and heat are

$$K_m = l S_m e^{1/2} \quad \text{and} \quad (6)$$

$$K_h = l S_h e^{1/2}, \quad (7)$$

where e is the TKE, l the turbulent master length scale, and the stability functions are represented by $S_{m,h}$.

In UWMT, TKE is diagnosed rather than prognosed, and TKE storage is neglected. The TKE balance equation differs according to the stability of the atmospheric layer. In a stable turbulent layer, turbulent transport of TKE is assumed to be small and is neglected, and the resulting TKE balance equation is

$$B + P_s + W - D = 0, \quad (8)$$

where B is buoyant production of TKE, P_s is shear production, W is the source of TKE from wind turbines [Eq. (4)], and D is the dissipation of TKE.

In a convective layer, turbulent transport of TKE is modeled as a relaxation to the turbulent layer–mean TKE [see Eq. (26) in Bretherton and Park 2009], and the TKE balance is

$$B + P_s + T_e + W - D = 0, \quad (9)$$

TABLE 1. List of the set of simulations performed in this study. The name of each simulation is accompanied by the type of parameterization (elevated momentum sink or enhanced surface roughness), installed capacity, turbine spacing, and whether turbine blade mixing is represented through enhanced TKE.

Name	Type	Installed capacity (TW)	Turbine spacing (rotor diameters)	Enhanced TKE
CTL	No wind turbines	—	—	—
WF	Elevated	10	8	Yes
WFD	Elevated	10	8	No
WFD2	Elevated	20	4	Yes
WFQ	Elevated	2.5	8	Yes
Z0	Surface	—	—	—

where T_e is the source of TKE from turbulent transport. The shear and buoyant production terms are computed as

$$P_s = -\overline{w'u'}\frac{\partial U}{\partial z} - \overline{w'v'}\frac{\partial V}{\partial z} \quad \text{and} \tag{10}$$

$$B_s = \overline{w'b'} = -K_h N^2, \tag{11}$$

where b' is the buoyancy perturbation and N^2 is the buoyancy frequency diagnosed from moist conserved variables.

The wind turbine parameterization reduces the wind within layers containing rotor blades, thus altering the vertical wind shear and the turbulent fluxes through Eq. (5). In addition, the source of TKE increases the eddy diffusivities [Eqs. (6) and (7)] and thus the vertical diffusion.

c. Model configuration

To explore the potential climate impact of large deployments of wind power across the globe in regionally high densities over land, we employed CAM5 in stand-alone mode with climatological sea surface temperatures. Finite-volume dynamics with a resolution of $0.9°$ latitude $\times$ $1.25°$ longitude and 30 levels in the vertical was used for all model runs. Two model levels intersect the rotor area. The model was integrated for 61 years in all cases to ensure a climatic steady state, using initial conditions from a prespun-up state. Greenhouse gas levels were kept constant at year 2000 levels to eliminate climate change impacts. The standard CAM5 physics parameterization suite was used (Neale et al. 2012); however, turbulent mountain stress was turned off to give a better prediction of near-surface winds over land in nonmountainous areas where the wind farms are located (see Fig. 2 from Lindvall et al. 2013).

The simulations conducted are listed in Table 1. The control (CTL) simulation does not contain any wind turbines and is used to compare with the other simulations to highlight the wind farm impacts. The remaining simulations include wind turbines, the effects of which are parameterized using two methods. The first method uses the elevated momentum sink parameterization,

described in section 2a. These experiments are named beginning with WF. The first wind farm (WF) experiment has a total installed capacity of 10 TW and uses a typical large modern wind turbine configuration, with a nominal power output of 5 MW, hub height of 100 m, and blade diameter of 126 m. The horizontal turbine density corresponds to a turbine spacing of 8 rotor diameters. The power and thrust coefficients incorporated into the model are from the commercial REpower 5M turbine (REpower 2014). The cut-in and cut-out wind speeds, below and above which the turbines do not operate, are 3.5 and $30\,\mathrm{m\,s^{-1}}$, respectively. Between the cut-in speed and $9\,\mathrm{m\,s^{-1}}$, the thrust coefficient is a maximum and mostly constant with wind speed. At higher wind speeds the thrust coefficient falls rapidly, where at $13\,\mathrm{m\,s^{-1}}$ it is approximately half the value than at lower speeds.

To explore the impact of turbine blade–generated TKE, a second experiment was performed, denoted by WFD. It has the same characteristics as the WF experiment described above; however, turbine-generated TKE is neglected, and the parameterization behaves as a momentum sink only. A further experiment, denoted by WFD2, explores the impact of a doubling in turbine density (corresponding to a turbine separation of 4 rotor diameters), with a total installed capacity of 20 TW. Additionally, to assess the impact of the area of the wind farms, the north–south and east–west dimensions of the wind farms are halved (thus keeping the same aspect ratio as the other experiments), corresponding to an area in size one-quarter that of WF. This experiment is denoted by WFQ and has a total installed capacity of 2.5 TW.

Finally, an additional method of representing wind farms is tested that has been used in previous global studies (Ivanova and Nadyozhina 2000; Keith et al. 2004; Kirk-Davidoff and Keith 2008; Barrie and Kirk-Davidoff 2010; Wang and Prinn 2010, 2011); that is, increasing the roughness length for momentum z_0 over the wind farm areas. This experiment is denoted by Z0. We follow Fitch et al. (2013b) and set $z_0 = 2.6$ m, representing wind turbines with moderate loading and of a similar size and spacing to those in WF (according to LES analysis by

Wind farm locations (WF, WFD, WFD2, Z0)
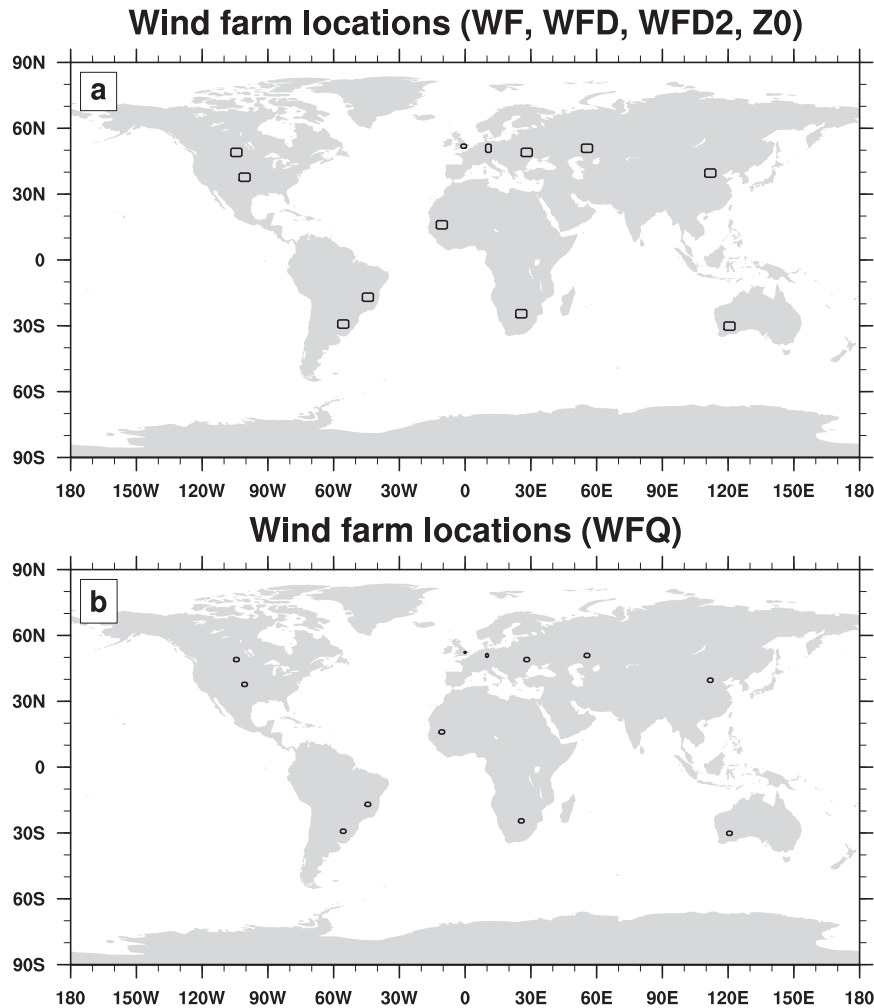

Wind farm locations (WFQ)

FIG. 1. Location of the wind farms in (a) the WF, WFD, WFD2, and Z0 cases and (b) the WFQ case.

Calaf et al. 2011). In addition, the displacement height over wind farm areas is set to zero. According to Calaf et al. (2011), the displacement height over wind turbines was found to be zero or close to zero. Figure 1a shows the location of wind turbines in WF, WFD, WFD2, and Z0. The location of wind turbines in WFQ is shown in Fig. 1b. The wind farms are located across the globe over land with a wide range of surface types and wind climate, which are expected to influence the magnitude of the wind farm impacts.

The first year of the simulations is discarded to eliminate spinup effects, and the results shown are means over a 60-yr period.

d. Coupling with the land surface model

CAM5 is coupled with a land surface model, the Community Land Model (CLM), version 4 (Oleson et al. 2010), which provides surface fluxes of momentum, and sensible and latent heat to CAM5. The fluxes are

calculated from Monin–Obukhov similarity theory. Here, we focus on the calculation of sensible heat flux, as Fitch et al. (2013b) found the increased sensible heat fluxes over wind farms represented by enhanced z_0 were mainly responsible for exaggerated near-surface temperatures. The sensible heat flux is calculated in CLM depending on whether the land surface is vegetated. For nonvegetated surfaces, the sensible heat flux H_g between the surface and the lowest model level at height z_{atm} is

$$H_g = -\rho_{atm} C_p \frac{(\theta_{atm} - T_g)}{r_{ah}}, \qquad (12)$$

where ρ_{atm} is the air density, C_p is the specific heat capacity of air, θ_{atm} is the potential temperature in the lowest model level, T_g is the ground temperature, and r_{ah} is the aerodynamic resistance to sensible heat transfer between the land and atmosphere. Other resistances for

momentum and moisture transfer are denoted as r_{am} and r_{aw}, respectively. These resistances depend on the surface roughness length. Owing to the differing transfer mechanisms for momentum, heat, and moisture, the roughness lengths may be different in each case. CLM employs the formulation from Zilitinkevich (1995) to compute the roughness lengths for heat and moisture. This approach was found in Fitch et al. (2013b) to produce the most reasonable heat fluxes and near-surface temperatures with the enhanced z_0 method. The roughness lengths over nonvegetated surfaces for heat $z_{0h,g}$ and moisture $z_{0w,g}$ are

$$z_{0h,g} = z_{0w,g} = z_{0m,g} \exp(-a u_* z_{0m,g}/\nu)^{0.5}, \quad (13)$$

where $z_{0m,g}$ is the roughness length for momentum and $u_* z_{0m,g}/\nu$ is the roughness Reynolds number, and ν is the kinematic viscosity of air and $a = 0.13$.

The aerodynamic resistance to sensible heat transfer between the land and atmosphere (r_{ah}) is

$$r_{ah} = \frac{1}{k^2 V_a} \left[\ln\left(\frac{z_{atm} - d}{z_{0m,g}}\right) - \Psi_m\left(\frac{z_{atm} - d}{L}\right) \right. $$
$$+ \Psi_m\left(\frac{z_{0m,g}}{L}\right) \left] \right[\ln\left(\frac{z_{atm} - d}{z_{0h,g}}\right) $$
$$\left. - \Psi_h\left(\frac{z_{atm} - d}{L}\right) + \Psi_h\left(\frac{z_{0h,g}}{L}\right) \right], \quad (14)$$

where V_a is the wind speed in the lowest model layer; k is the von Kármán constant; d is the displacement height; L is the Monin–Obukhov length scale; and Ψ_m and Ψ_h are Monin–Obukhov stability functions, which augment the resistance depending on the stability in the surface layer. From this equation, it can be seen that if the roughness lengths for momentum and heat ($z_{0m,g}$ and $z_{0h,g}$) are increased, the resistance to sensible heat transfer will be reduced, in turn increasing the sensible heat flux [Eq. (12)].

For vegetated surfaces, the sensible heat flux is partitioned into vegetation and ground fluxes, such that the sensible heat flux H between the surface and the atmosphere is balanced by the sum of the sensible heat from the vegetation (H_v) and the ground (H_g):

$$H = H_v + H_g, \quad (15)$$

where

$$H = -\rho_{atm} C_p \frac{(\theta_{atm} - T_s)}{r_{ah}}, \quad (16)$$

$$H_v = -\rho_{atm} C_p (T_s - T_v) \frac{L + S}{r_b}, \quad \text{and} \quad (17)$$

$$H_g = -\rho_{atm} C_p \frac{(T_s - T_g)}{r'_{ah}}, \quad (18)$$

where T_s is the canopy air temperature, L and S are the exposed leaf and stem area indices, r_b is the leaf boundary layer resistance, and r'_{ah} is the aerodynamic resistance to heat transfer between the ground and the canopy air. The reader is referred to Oleson et al. (2010) for further details. The extra resistances r_b and r'_{ah} are important for reducing the sensible heat flux to the atmosphere with the enhanced z_0 method for representing wind farms, which will be discussed later.

3. Results

a. Vertical profiles above a wind farm

The behavior of the different wind farm parameterizations and the response to various configurations of wind turbines is highlighted through analyzing the mean vertical profiles over the wind farm areas. In the WF, WFD2, and WFQ cases, the wind farm parameterization directly influences both wind speed (momentum) and TKE. The WFD and Z0 cases directly influence wind speed only. Vertical mean profiles of the difference in wind speed and TKE over one of the most productive wind farms (located in Canada) over a 60-yr period are shown in Fig. 2. There is a maximum decrease in the wind speed of $0.8 \, \text{m s}^{-1}$ and an increase in TKE of $0.16 \, \text{m}^2 \, \text{s}^{-2}$ in the WF case, corresponding to a decrease of 18% and an increase of 40%, respectively, relative to CTL. As there is no direct representation of turbine blade mixing in WFD, the maximum increase in TKE is reduced by approximately 50% relative to WF. In both cases, the momentum deficit within the wind farm increases the vertical wind shear and thus shear production of TKE above the rotor area. However, as there is no direct addition of TKE within the rotor area in WFD (to represent mixing by the turbine blades), the TKE is reduced both within and above the wind farm relative to WF. The momentum deficit in the wind farm reduces the wind shear near the ground, thus reducing shear production of TKE at lower levels in WFD, with a maximum reduction of $0.12 \, \text{m}^2 \, \text{s}^{-2}$ (22%) in TKE relative to CTL. The representation of TKE is in general important, as the wind speed deficit within large farms is replenished primarily by vertical turbulent mixing of momentum (Calaf et al. 2011; Fitch et al. 2013a). However, the impact of enhanced TKE has a reduced impact on wind deficits in this study compared with the high-resolution simulations of Fitch et al. (2012), most likely owing to the much coarser vertical resolution employed here. The increased TKE in WF (with respect to WFD) leads to
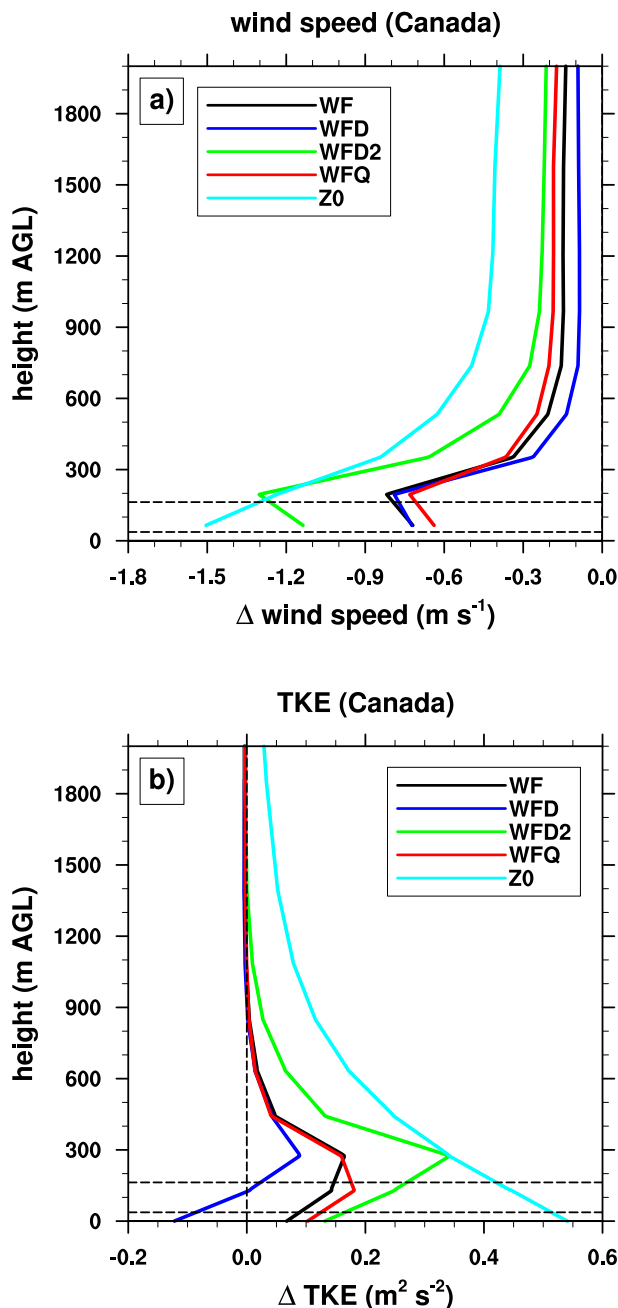
wind speed (Canada)

TKE (Canada)

FIG. 2. Vertical mean profiles over the wind farm in Canada for each case over a 60-yr period: (a) difference in wind speed with respect to CTL and (b) difference in TKE with respect to CTL. Horizontal dashed lines indicate the rotor area.

slightly greater momentum deficits above the rotor area where faster flow has been more efficiently mixed down. With greater TKE in WFQ, this effect is slightly more pronounced.

A doubling in the wind turbine density (represented in the WFD2 case) increases the extraction of KE and thus leads to a greater reduction in the wind of $1.3 \, \mathrm{m \, s^{-1}}$

relative to CTL, a decrease of 29%. The shear production of TKE above the rotor area is enhanced, with a maximum increase in TKE of $0.35 \, \mathrm{m^2 \, s^{-2}}$, an increase of 88% relative to CTL. The TKE within the rotor area is also increased relative to WF by approximately 67%.

A smaller wind farm with an area one-quarter that of WF (represented in the WFQ case) causes a smaller reduction in the wind of $0.7 \, \mathrm{m \, s^{-1}}$ relative to CTL, a reduction of 16%. However, the TKE is increased compared to WF, with a maximum increase in TKE of $0.18 \, \mathrm{m^2 \, s^{-2}}$, an increase of 37% relative to CTL. The smaller momentum deficit within the farm leads to greater turbine-generated TKE [through the dependence on $|\mathbf{V}|^3$ in Eq. (4)].

Finally, the Z0 case is compared, where wind turbines are instead represented as an increase in z_0 rather than an elevated momentum sink. The Z0 case shows the greatest reduction in wind speed of all the cases, with a maximum reduction of $1.5 \, \mathrm{m \, s^{-1}}$, a reduction of 44% relative to CTL. The maximum wind speed reduction is nearly a factor of 2 greater than WF. Although the roughness length chosen is supposed to be characteristic of a similar turbine spacing as in WF, it more closely follows the wind profile of WFD2, where the turbine density is doubled. The Z0 case also exhibits the greatest increase in TKE of all the cases, with a maximum increase in TKE of $0.55 \, \mathrm{m^2 \, s^{-2}}$, an increase by a factor of 2 relative to CTL. This production of TKE is more than 3 times that of WF. In Z0, the TKE is also greatest near the ground, contrasting with the other cases where the maximum in TKE is seen within or above the rotor area. The enhanced surface roughness in the Z0 case increases shear production of TKE mostly near the surface.

b. Influence on wind speed and TKE

Wind farms extract KE from the mean flow to produce electrical power, thus reducing the wind speed both within the wind farm and downstream in the wake. The mean influence of the wind farms on wind speed at hub height [100 m above ground level (AGL)] across the globe over a 60-yr period in the WF case can be seen in Fig. 3a. Stippling indicates points that are significant at the 95% level using a Student's t test on annual means. For reference, the mean wind speed at hub height in CTL is shown in Fig. 4. The influence on wind speed is mostly confined to the wind farm areas and immediate surroundings. Wind speed changes elsewhere are less than $0.4 \, \mathrm{m \, s^{-1}}$. A maximum decrease in the wind of $1.3 \, \mathrm{m \, s^{-1}}$ is seen within the wind farm areas. The smaller wind farms in the United Kingdom and Germany show a smaller decrease in the wind as there are fewer wind turbines to extract KE from the flow. These wind farms do not display
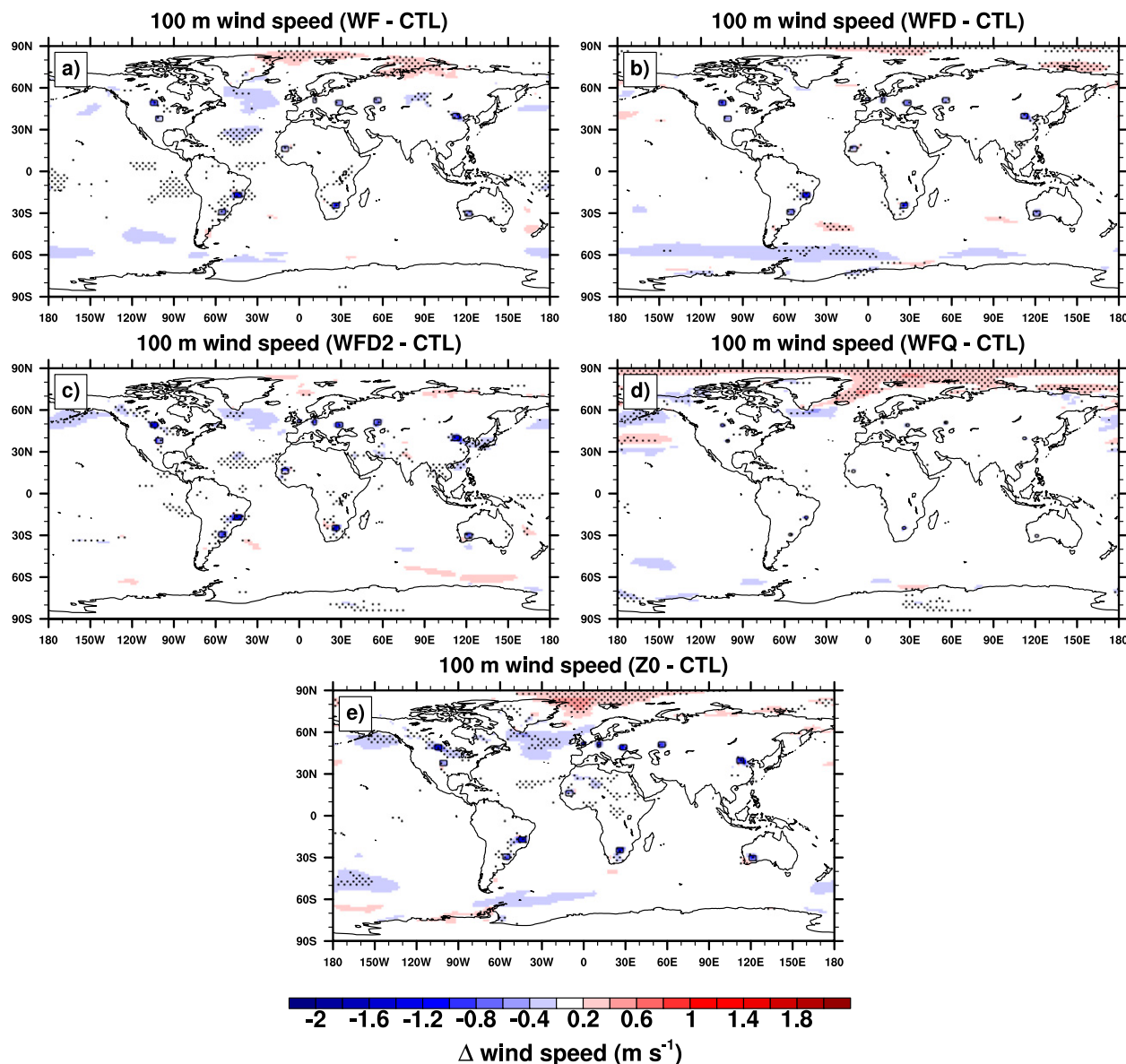
FIG. 3. Mean difference in wind speed at hub height (100 m AGL) over a 60-yr period for each case with respect to CTL: (a) WF case, (b) WFD case, (c) WFD2 case, (d) WFQ case, and (e) Z0 case. Wind farm locations are indicated by black rectangles. Stippling indicates points that are significant at the 95% level using a Student's t test on annual means.

any significant changes in the wind speed in the surrounding areas. Downstream impacts are most significant in the regions around the wind farms in China and northern Brazil. The WFD case (Fig. 3b) shows similar impacts to the WF case; however, the wind speed is further reduced over the wind farms in the United Kingdom and Germany. The wind speed is reduced by 0.4–0.6 m s^{-1} from less than 0.4 m s^{-1} in these wind farms. When the wind turbine density is doubled (Fig. 3c), the wind speed is further reduced over all the wind farm areas, and wake effects become more noticeable. Substantial wakes can be seen in North America, China, and Brazil. Wake effects are

minimal over Europe. Reducing the wind farm areas to a quarter of that in the other cases (Fig. 3d) shows minimal wake effects, and the reduction in wind is confined mostly to the wind farm areas. Outside these areas, the change in wind speed is mostly less than 0.4 m s^{-1}. The greatest reduction in the wind is seen in the Z0 case (Fig. 3e), where wind farm areas are instead represented as an increase in surface roughness. Wake effects are exaggerated with respect to WF, and impacts outside the wind farm areas are also increased but remain less than 0.6 m s^{-1}.

The overall impact on wind speed within the wind farm areas is highlighted in Fig. 5a. The mean wind speed
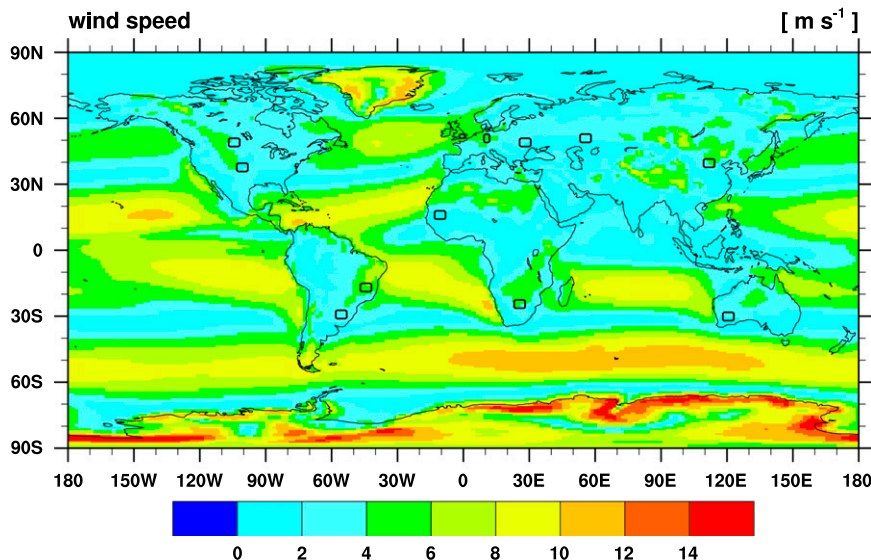
FIG. 4. Mean wind speed at hub height (100 m AGL) over a 60-yr period for CTL. Wind farm
locations are indicated by black rectangles.

reduction over a 60-yr period within the wind farm areas for the WF, WFD, WFD2, WFQ, and Z0 cases is 0.61, 0.62, 0.92, 0.49, and 0.92 m s^{-1}, respectively. In the WF case, the wind speed reduction is mostly within the range of 0.4 to 0.8 m s^{-1}, with a mean reduction of 19.0%. Slightly greater wind speed deficits are seen in WFD, with a mean reduction of 19.3%. The increased turbine density in WFD2 causes a greater reduction in the wind, with a decrease mostly within the range of 0.6–1.2 m s^{-1} with a mean reduction of 28.8%, a 50% increase relative to WF. With fewer turbines to reduce the KE in the wake, the WFQ case shows the smallest decrease in the wind, with a reduction mostly between 0.4 and 0.6 m s^{-1} and a mean reduction of 15.5%. The Z0 case is similar to WFD2, with slightly larger wind speed deficits. Mean impacts, both within the wind farm areas only and over the entire globe, are summarized in Table 2. The mean global impact on wind speed is very slight; less than 0.7% in all cases. The uncertainty is larger than the magnitude of change for all the cases, apart from WF and Z0, where there is an overall slight reduction in wind speed. In the table the 95% confidence intervals are given, which are calculated as 1.96 multiplied by the standard deviation of the annual mean divided by the square root of the number of years (60 years).

Impacts on TKE are limited to within the wind farm areas only (not shown), with a mean increase in TKE at hub height (100 m AGL) over all the wind farms of 0.09 m^2 s^{-2} in the WF case, corresponding to an increase of 17% relative to CTL (Fig. 5b). The reduced near-surface wind shear and omission of turbine blade mixing in WFD reduces the TKE at hub height within the wind farms relative to CTL by 0.03 m^2 s^{-2}, or 6%. Relative to

WF, the TKE is decreased by 23%. The reduced TKE in WFD increases the momentum deficit within the wind farms slightly. Doubling the turbine density in WFD2 generates more TKE within the wind farms, with a mean increase of 0.15 m^2 s^{-2}, a 30% increase relative to CTL and nearly a factor of 2 greater than the increase seen in WF. The smaller wind farms in WFQ reduce wake effects on downstream turbines, leading to increased production of TKE, relative to WF, with a mean increase in TKE of 0.13 m^2 s^{-2}, a 25% increase relative to CTL. The Z0 case shows the greatest enhancement in TKE of all the cases, with a mean increase of 0.29 m^2 s^{-2}, a 56% increase relative to CTL and a factor of 3 greater than the TKE increase in WF. In Z0 the enhanced surface roughness leads to large shear production of TKE near the surface.

c. Influence on temperature

Much interest has been generated recently on the potential for wind farms to impact air temperatures. Wind turbines may mix warmer θ air downward and cooler θ air upward during stable conditions, leading to a warming at low levels. The opposite may occur during unstable conditions (Fitch et al. 2013a). The mean influence of the wind farms on the lowest model level temperature across the globe over a 60-yr period in the WF case can be seen in Fig. 6a. Stippling indicates points that are significant at the 95% level using a Student's t test on annual means. Temperature changes of less than 0.5 K are seen and are mostly confined to the wind farm areas and immediate surroundings. Half of the wind farms display a warming, mostly below 0.25 K. The other half displays no significant changes in temperature, with
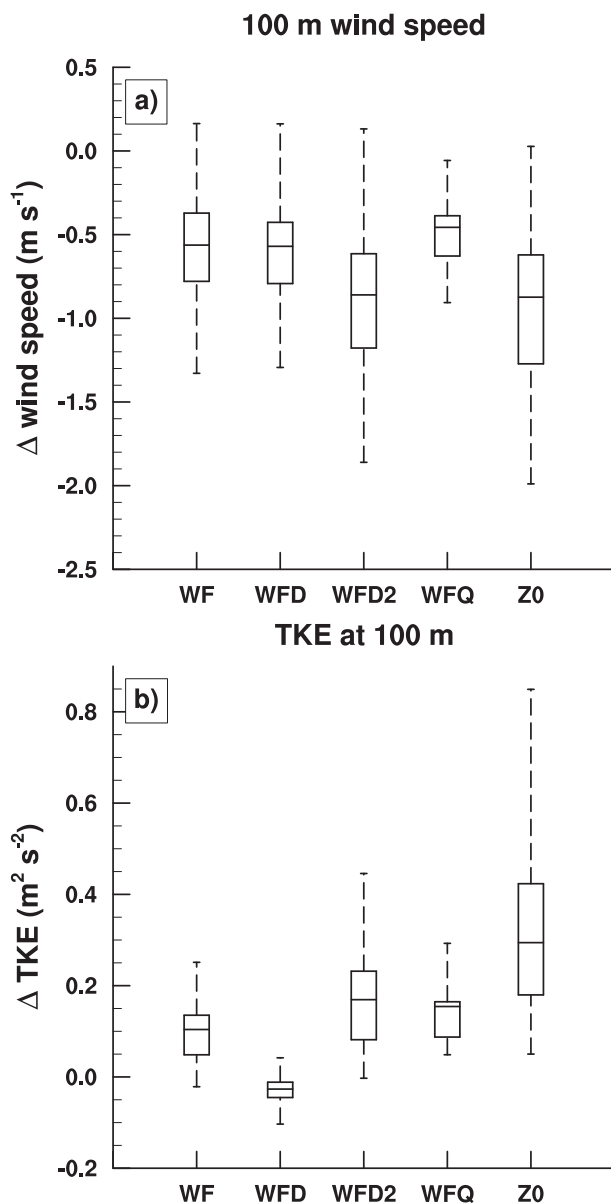
FIG. 5. Box plot of the mean difference over the wind farm areas for a 60-yr period for each case with respect to CTL for (a) wind speed at hub height and (b) TKE at hub height. The minimum, first quartile, median, third quartile, and maximum values are indicated.

the exception of the wind farm in Canada, where a cooling of up to 0.5 K is seen at the prevailing upstream edge of the wind farm. In WFD, the warming over the wind farms in South Africa and Australia is increased slightly, relative to WF, to a maximum of 0.6 K (Fig. 6b). The cooling over the wind farm in Canada is reduced. A doubling in the wind turbine density (WFD2) increases the temperature changes, with a maximum warming and cooling of 0.7 and 0.5 K, respectively (Fig. 6c). There is a region of cooling around the wind farms in Eastern

Europe and Central Asia of mostly less than 0.4 K. The increase in TKE production in WFD2 is likely responsible for the increased warming over the wind farms, with respect to WF, owing to the increased vertical turbulent mixing. Temperature changes are very small in WFQ (Fig. 6d), where the wind farm areas are a quarter of the size of WF. A maximum warming of 0.4 K is seen over some of the wind farm areas. In the Z0 case, the warming over the wind farms in western Africa, China, and Australia is increased relative to WF, with a maximum warming of 0.8 K (Fig. 6e). The warming over the wind farms in South America and South Africa is reduced with respect to WF. Temperatures are increased the most over wind farms where the underlying surface is more than 30% nonvegetated (not shown; i.e., the wind farms in western Africa, China, and Australia). In these cases, the surface heat fluxes are increased through the lower resistance to heat transfer between the land and atmosphere [Eq. (14)] due to the increased roughness lengths for momentum and heat, which in turn increase the near-surface temperatures. For vegetated surfaces, the extra resistances in Eqs. (17) and (18) apply, which act to offset the lowered resistance in Eq. (14), thus moderating the surface heat fluxes. In addition, the displacement height is set to zero over the wind farm areas, a change from nonzero (for vegetated surfaces only), further increasing the resistance to heat transfer over vegetated surfaces [Eq. (14)]. The Z0 case shows the greatest influence of all the cases on temperatures beyond the wind farm areas, with temperature changes greater in magnitude and area. However, temperature changes remain less than ±0.6 K.

The overall temperature impact within the wind farms in the lowest model level is summarized in Fig. 7a. The mean temperature increase over a 60-yr period in the WF, WFD, WFD2, WFQ, and Z0 cases is 0.09, 0.12, 0.16, 0.12, and 0.09 K, respectively. The maximum temperature change is less than 0.8 K in all cases.

The local- (over the wind farm areas only) and global-mean temperature impacts are given in Table 2. The global temperature change is extremely slight, and the uncertainty is larger than the mean value in all cases apart from WFD2, which shows a very slight cooling.

d. Influence on sensible and latent heat fluxes

Impacts on sensible and latent heat fluxes are a particular concern for agriculture, as they directly influence near-surface temperature and humidity. In all cases apart from Z0, the wind farms have only a small influence on the sensible heat fluxes, with most changes insignificant at the 95% level. Changes become more significant in WFD2 and Z0. The sensible heat flux changes primarily through changes in the temperature

TABLE 2. Mean impacts locally within the wind farm areas and globally over a 60-yr period for each case with respect to CTL for lowest model level temperature; wind speed at hub height (100 m AGL); wind direction at hub height; TKE at hub height; sensible and latent heat flux; low cloud fraction; and total precipitation rate. The change in wind direction is negative in the Northern Hemisphere and positive in the Southern Hemisphere. The 95% confidence intervals given are calculated from annual means (described in section 3b).

		WF	WFD	WFD2	WFQ	Z0
Temperature (K)	Local	+0.09 ± 0.07	+0.12 ± 0.06	+0.16 ± 0.09	+0.12 ± 0.07	+0.09 ± 0.07
	Global	−0.009 ± 0.014	−0.008 ± 0.013	−0.017 ± 0.016	−0.013 ± 0.015	−0.003 ± 0.016
Wind speed (%)	Local	−19.0 ± 1.4	−19.3 ± 1.3	−28.8 ± 1.2	−15.5 ± 1.3	−28.8 ± 1.2
	Global	−0.64 ± 0.56	−0.42 ± 0.51	−0.41 ± 0.52	−0.17 ± 0.55	−0.67 ± 0.56
Wind direction (°)	Local	±7.0 ± 0.7	±6.8 ± 0.7	±9.6 ± 0.7	±3.7 ± 0.7	±5.9 ± 0.7
TKE (%)	Local	+17 ± 0.8	−6 ± 0.7	+30 ± 1.0	+25 ± 0.9	+56 ± 0.8
Sensible heat flux (%)	Local	−0.5 ± 1.3	+0.5 ± 1.1	−1.4 ± 1.2	+1.4 ± 1.2	+0.8 ± 1.3
	Global	+0.5 ± 0.2	+0.5 ± 0.2	+0.6 ± 0.2	+0.7 ± 0.2	+0.8 ± 1.3
Latent heat flux (%)	Local	+0.4 ± 0.2	−0.3 ± 1.0	+0.5 ± 1.0	−0.8 ± 1.0	+5.3 ± 1.0
	Global	−0.06 ± 0.09	−0.11 ± 0.07	−0.08 ± 0.07	−0.09 ± 0.08	0.01 ± 0.08
Low cloud fraction (%)	Local	+0.7 ± 0.3	+0.6 ± 0.2	+1.0 ± 0.3	+0.3 ± 0.3	+1.0 ± 0.3
	Global	+0.2 ± 0.04	+0.2 ± 0.03	+0.2 ± 0.04	+0.2 ± 0.04	+0.004 ± 0.04
Total precipitation rate (%)	Local	+2.6 ± 1.5	+1.3 ± 0.007	+3.4 ± 1.6	+0.3 ± 1.6	+6.0 ± 1.7
	Global	−0.06 ± 0.09	−0.11 ± 0.07	−0.08 ± 0.07	−0.09 ± 0.08	+0.01 ± 0.08

contrast between the lowest atmospheric layer and the surface [$(\theta_{atm} - T_g)$ in Eq. (12)] and changes in wind speed in the lowest atmospheric layer [V_a in Eq. (14)]. A greater temperature contrast will result in larger sensible heat fluxes, and higher wind speeds act to reduce the resistance to heat transfer, in turn increasing the fluxes. In wind farms, vertical turbulent mixing may change the temperature near the surface (Fitch et al. 2013a,b) and in turn the sensible heat fluxes. The reduction in wind speed acts to reduce the sensible heat fluxes.

In the WF case, there is a slight decrease in the mean sensible heat flux of $-0.21 \, \mathrm{W \, m^{-2}}$ within the wind farm areas over a 60-yr period (Fig. 7b), corresponding to a decrease of 0.5%. The maximum change in the sensible heat flux is mostly less than $\pm 1 \, \mathrm{W \, m^{-2}}$. Some grid cells show maximum changes in the sensible heat flux of up to 3.6 and $-4.8 \, \mathrm{W \, m^{-2}}$. In the WFD case, the mean sensible heat flux increases slightly by $0.17 \, \mathrm{W \, m^{-2}}$, an increase of 0.5% relative to CTL. The maximum change in the fluxes is still mostly less than $\pm 1 \, \mathrm{W \, m^{-2}}$. The absolute maximum change is reduced with respect to WF. Doubling the density of wind turbines (WFD2, Fig. 7b) increases the change in sensible heat fluxes, with a maximum increase and decrease of 4.3 and $-6.6 \, \mathrm{W \, m^{-2}}$, respectively. The mean change in sensible heat flux over the wind farm areas is $-0.53 \, \mathrm{W \, m^{-2}}$, a decrease of 1.4% relative to CTL and more than a factor of 2 greater than the reduction in WF. The WFQ case shows the smallest range in sensible heat flux change of all the cases, with a maximum increase and decrease of 3.5 and $-2.2 \, \mathrm{W \, m^{-2}}$, respectively. However, the mean sensible heat flux is increased slightly by $0.53 \, \mathrm{W \, m^{-2}}$, an increase of 1.4%. The greatest changes in sensible heat flux are seen in the

Z0 case, with a maximum increase and decrease of 5.4 and $-9.2 \, \mathrm{W \, m^{-2}}$, respectively, corresponding to changes of up to 24%. The mean change is $+0.32 \, \mathrm{W \, m^{-2}}$, an increase of 0.8%. As discussed in the previous section, the sensible heat fluxes are directly increased over some wind farms through the reduced resistance to heat transfer. Outside the wind farm areas, there is little significant change in sensible heat flux (not shown). There is a slight increase in the global-mean sensible heat flux in all the cases, with an increase of 0.5% in the WF case (Table 2).

Differences in latent heat fluxes between the wind farm and CTL cases over the wind farm areas are summarized in Fig. 7c. In the WF case, the latent heat flux changes mostly within $\pm 1 \, \mathrm{W \, m^{-2}}$, and there is a slight increase in the mean flux of $+0.16 \, \mathrm{W \, m^{-2}}$, an increase of 0.4%. The maximum increase and decrease is 3.8 and $-3.6 \, \mathrm{W \, m^{-2}}$, respectively. Neglecting turbine blade mixing in WFD slightly decreases the mean flux by $0.11 \, \mathrm{W \, m^{-2}}$, a decrease of 0.3%. Doubling the turbine density (WFD2) increases the range of latent heat flux change, with a maximum increase and decrease of 6.0 and $-5.0 \, \mathrm{W \, m^{-2}}$, respectively. The mean change is $+0.19 \, \mathrm{W \, m^{-2}}$, an increase of 0.5%. Smaller wind farm size in WFQ reduces the maximum increase and decrease in latent heat fluxes the most, and there is an overall slight reduction in the mean of $0.29 \, \mathrm{W \, m^{-2}}$, a reduction of 0.8%. The greatest latent heat flux changes are seen in Z0, with a maximum increase and decrease of 9.0 and $-3.6 \, \mathrm{W \, m^{-2}}$, respectively. The mean change is $+2.0 \, \mathrm{W \, m^{-2}}$, an increase of 5.3%. In the Z0 case, the surface heat fluxes are increased directly through the enhanced surface roughness, discussed above. Outside the wind farm areas, changes in latent heat fluxes are small and there is no consistent
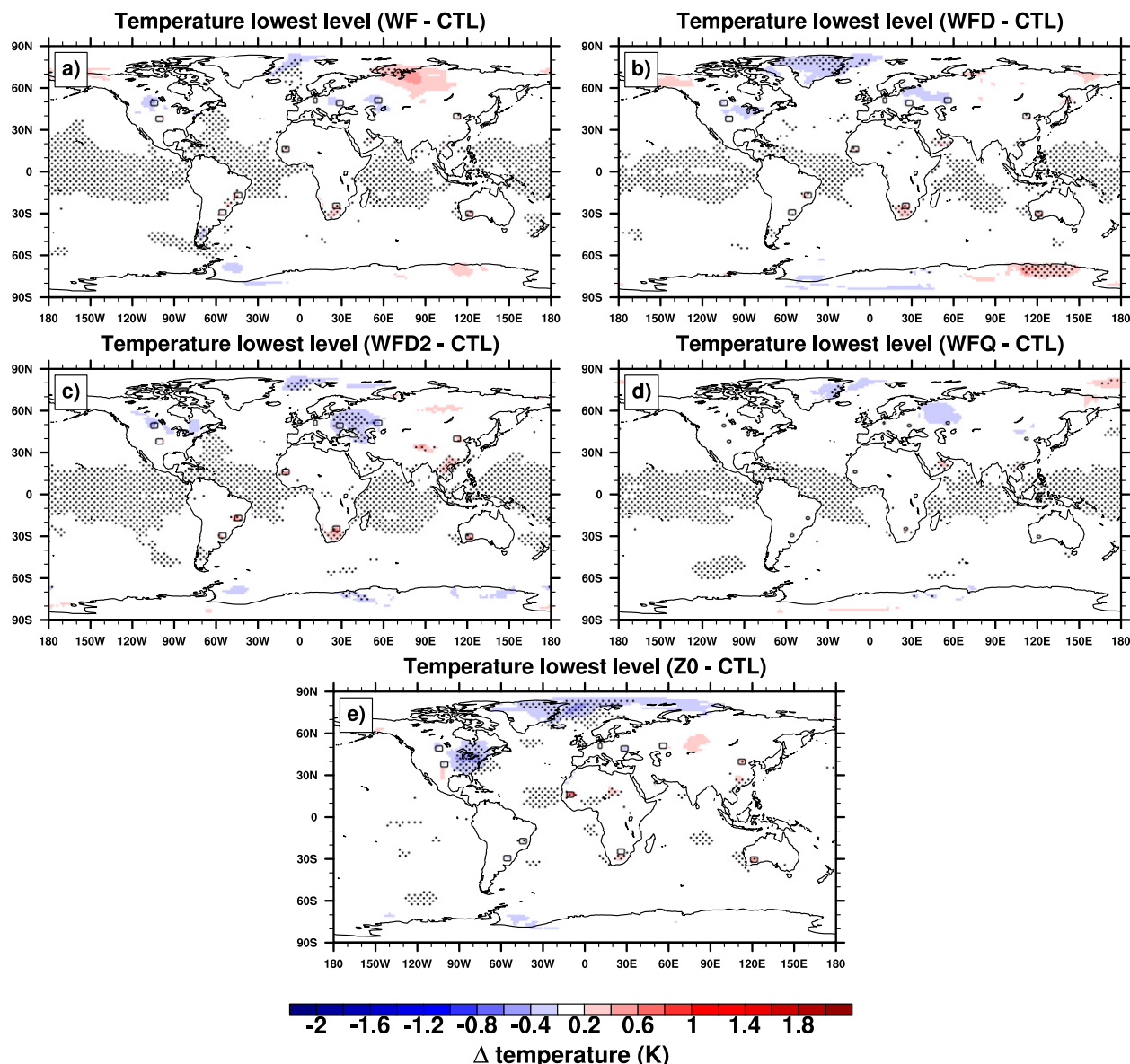
FIG. 6. Mean difference in temperature in the lowest model level over a 60-yr period for each case with respect to CTL: (a) WF case, (b) WFD case, (c) WFD2 case, (d) WFQ case, and (e) Z0 case. Wind farm locations are indicated by black rectangles. Stippling indicates points that are significant at the 95% level using a Student's *t* test on annual means.

pattern of change (not shown). The global-mean change is very slight in all the cases (Table 2).

e. Influence on cloud and precipitation

The low cloud amount is found to increase very slightly over the wind farm areas, with respect to CTL, as a result of flow convergence and uplift at the upstream edge (with respect to the prevailing flow) of the wind farms. Adiabatic cooling in the region of uplift increases the relative humidity and cloud fraction. Low cloud fraction is defined as the cloud fraction at levels lower

than 700 hPa. Conversely, there is a very slight decrease in low cloud fraction at the downstream edge of the wind farms, where flow divergence in the wake forces subsidence and adiabatic warming, in turn reducing the relative humidity and cloud amount. This mechanism is highlighted in Fig. 8a, which shows the mean change in cloud fraction and vertical pressure velocity (ω) over 60 years above the wind farm in Germany. Where the mean westerly flow impinges on the upstream edge of the wind farm, there is convergence and uplift (indicated by negative ω) and a slight increase in the cloud fraction of
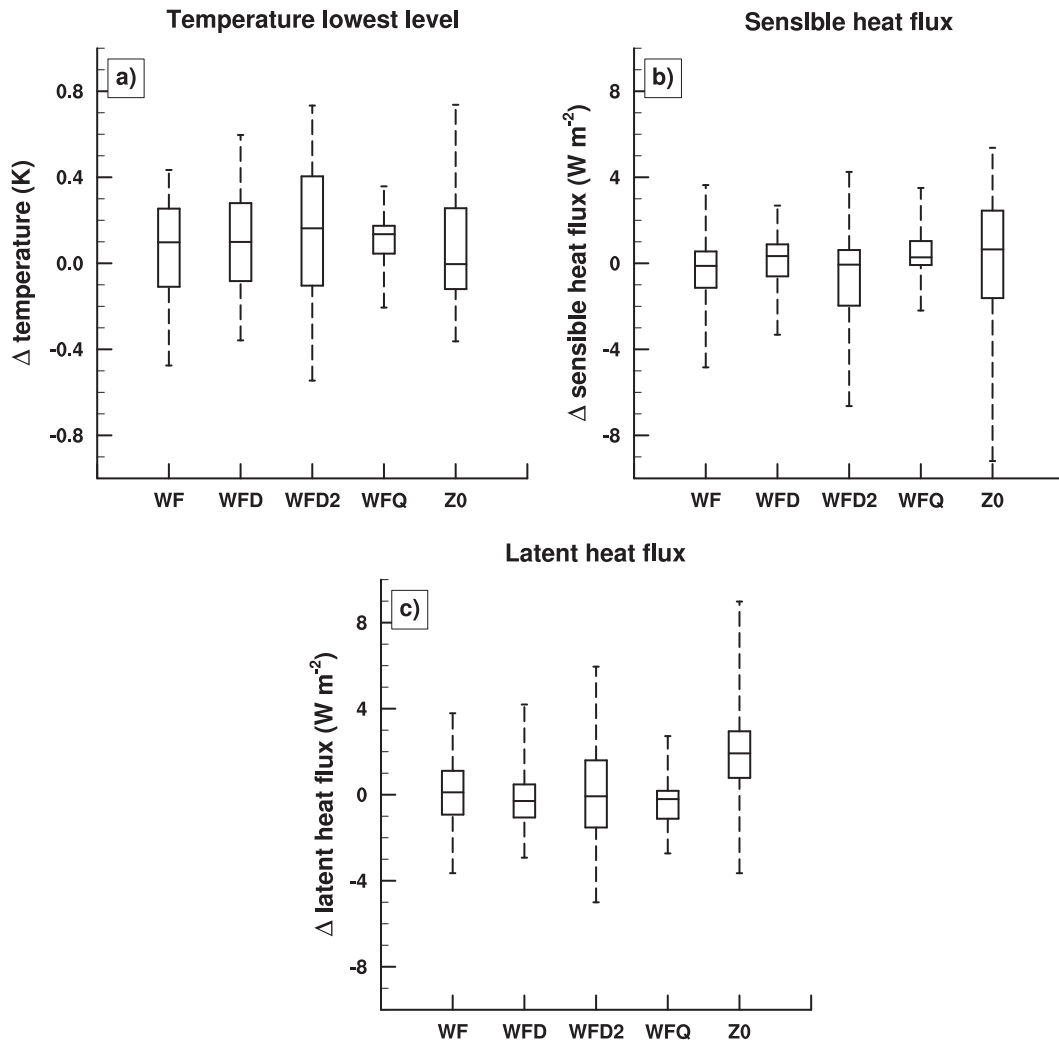
FIG. 7. Box plot of the mean difference over the wind farm areas for a 60-yr period for each case with respect to CTL for (a) temperature in the lowest model level, (b) sensible heat flux, and (c) latent heat flux. The minimum, first quartile, median, third quartile, and maximum values are indicated.

1%. Subsidence at the rear of the farm slightly decreases the cloud fraction by 1%. Doubling the density of turbines in WFD2 (Fig. 8b) further reduces the wind speed within the farm, causing greater flow convergence at the upstream edge of the farm, increasing the amount of uplift and subsidence by a factor of 2 (reflected by the ω values in Fig. 8b). In turn, the areas of cloud fraction increase/decrease are slightly enhanced. There is a maximum increase and decrease in the low cloud fraction of 1.5% and 2.8%, respectively.

The overall impact on low cloud fraction in the different cases is shown in Fig. 9a. In the WF case the mean change in low cloud fraction over the wind farm areas is +0.7%, with a maximum increase and decrease of 2.8% and 1.4%, respectively. Changes in cloud fraction are mostly less than 1%. Neglecting turbine blade

mixing in WFD slightly enhances the change in cloud fraction; however, the mean change over the wind farm areas remains similar at +0.6%. The change in low cloud fraction is enhanced the most in WFD2, where the turbine density is doubled. The mean change over the wind farm areas is +1%, with a maximum increase and decrease of 4.9% and −2.4%, respectively. The smallest changes in cloud fraction are seen in WFQ, where the wind farm size is reduced. In this case, smaller wind speed deficits within the wind farms reduce convergence and uplift and in turn changes in cloud fraction. The mean change in low cloud fraction over the wind farm areas is 0.3%, with a maximum increase and decrease of 1.5% and −1.1%, respectively. Similar changes in low cloud fraction are seen in Z0 as in WFD2, with a mean change in cloud fraction of +1% over the wind farm

Cloud fraction (WF - CTL)
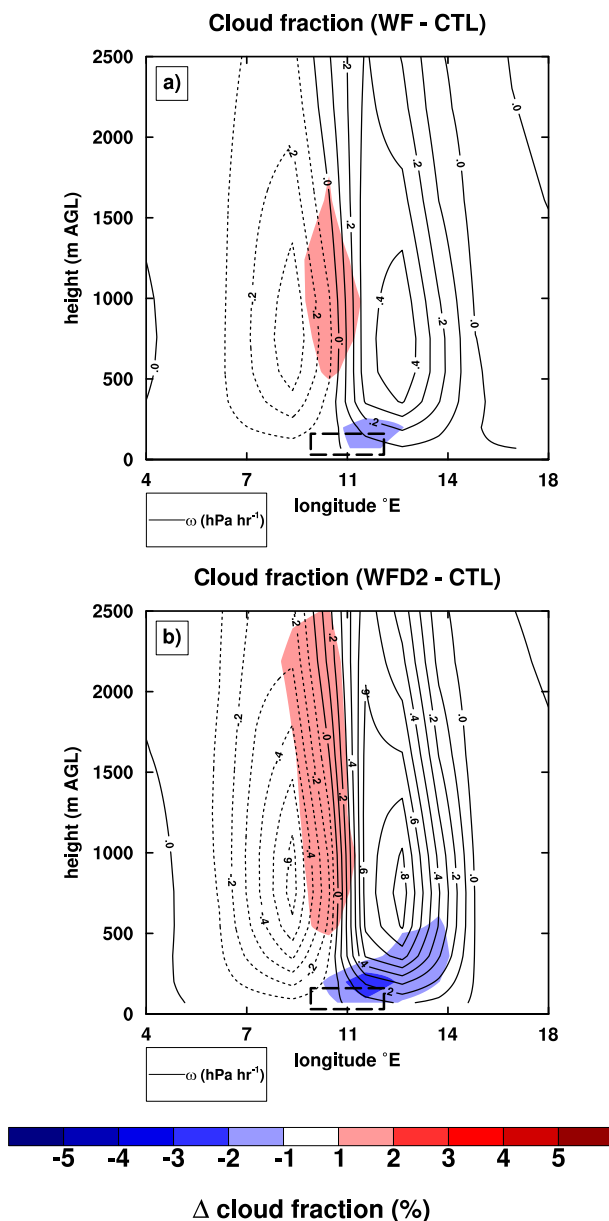

Cloud fraction (WFD2 - CTL)

FIG. 8. Vertical mean cross sections along the west–east direction over the wind farm in Germany for a 60-yr period showing the difference in cloud fraction and ω with respect to CTL for (a) the WF case and (b) the WFD2 case. Thick dashed lines indicate the wind farm area. The mean cross section over the wind farm in the north–south direction is shown.

areas. In this case, the wind speed deficit is further reduced with respect to WF, similarly to WFD2, increasing convergence and uplift. There is a slight increase in the global-mean low cloud fraction in all the cases, with an increase of 0.2% in the WF case (Table 2).

The slight increase in cloud fraction over the wind farms is reflected in the precipitation, with small increases in the total precipitation rate (Fig. 9b). In the

WF case, the mean change in total precipitation rate over the wind farm areas is $+14 \, \text{mm yr}^{-1}$, with a maximum increase and decrease of 65 and $-55 \, \text{mm yr}^{-1}$, respectively. The mean increase in precipitation over the wind farm areas corresponds to a 2.6% increase with respect to CTL. Neglecting turbine blade mixing in WFD reduces the mean precipitation rate change to $+7 \, \text{mm yr}^{-1}$, an increase of 1.3% relative to CTL. A doubling in the turbine density in WFD2 increases the mean precipitation rate by $19 \, \text{mm yr}^{-1}$, an increase of 3.4%, with a maximum increase and decrease of 91 and $-67 \, \text{mm yr}^{-1}$, respectively. The increase in precipitation with respect to WF is consistent with the increased low cloud amount discussed previously. The smallest change in precipitation rate is seen in WFQ, where the wind farm size is reduced, with a mean change in precipitation rate of $+2 \, \text{mm yr}^{-1}$, an increase of 0.3%. This reduction in precipitation with respect to WF is again consistent with the reduced low cloud amount. The greatest increase in precipitation rate is seen in Z0, with a mean change of $+33 \, \text{mm yr}^{-1}$, an increase of 6% relative to CTL and a factor of 2 greater than the increase in WF. The maximum increase and decrease is 122 and $-42 \, \text{mm yr}^{-1}$, respectively. The global-mean change in precipitation is slight in all the cases and not greater than 0.1% (Table 2).

The downwelling shortwave radiation flux is slightly reduced over the wind farm areas as a result of the increase in cloud fraction, with a mean reduction of $0.8 \, \text{W m}^{-2}$ in the WF case (Fig. 9c). Higher cloud fractions in WFD2 decrease the shortwave radiation flux further, with a mean reduction of $1.4 \, \text{W m}^{-2}$ relative to CTL. Reductions in WFQ are much smaller at $0.06 \, \text{W m}^{-2}$ as a result of the smaller increase in cloud fraction. The Z0 case shows the greatest impact, with a mean reduction of $2.4 \, \text{W m}^{-2}$ over the wind farm areas.

f. Influence on wind direction

The wind farms have a small impact on the wind direction, both within the wind farms and downstream in the wake. The forces acting in the boundary layer can be understood as an approximate balance between the pressure gradient force, the Coriolis force, and the turbulent drag (Holton 2004). Wind farms act to increase the turbulent drag, in turn increasing the velocity component directed toward lower pressure. As a result, the wind farms cause the wind to turn to the left of the geostrophic wind in the Northern Hemisphere and to the right in the Southern Hemisphere, with respect to CTL (not shown). The degree of wind turning among the wind farms is found to be dependent on the static stability in the lowermost layers of the atmosphere where the wind turbines are located (Fig. 10a). Among the wind farms, little correlation is found between the

Low cloud fraction

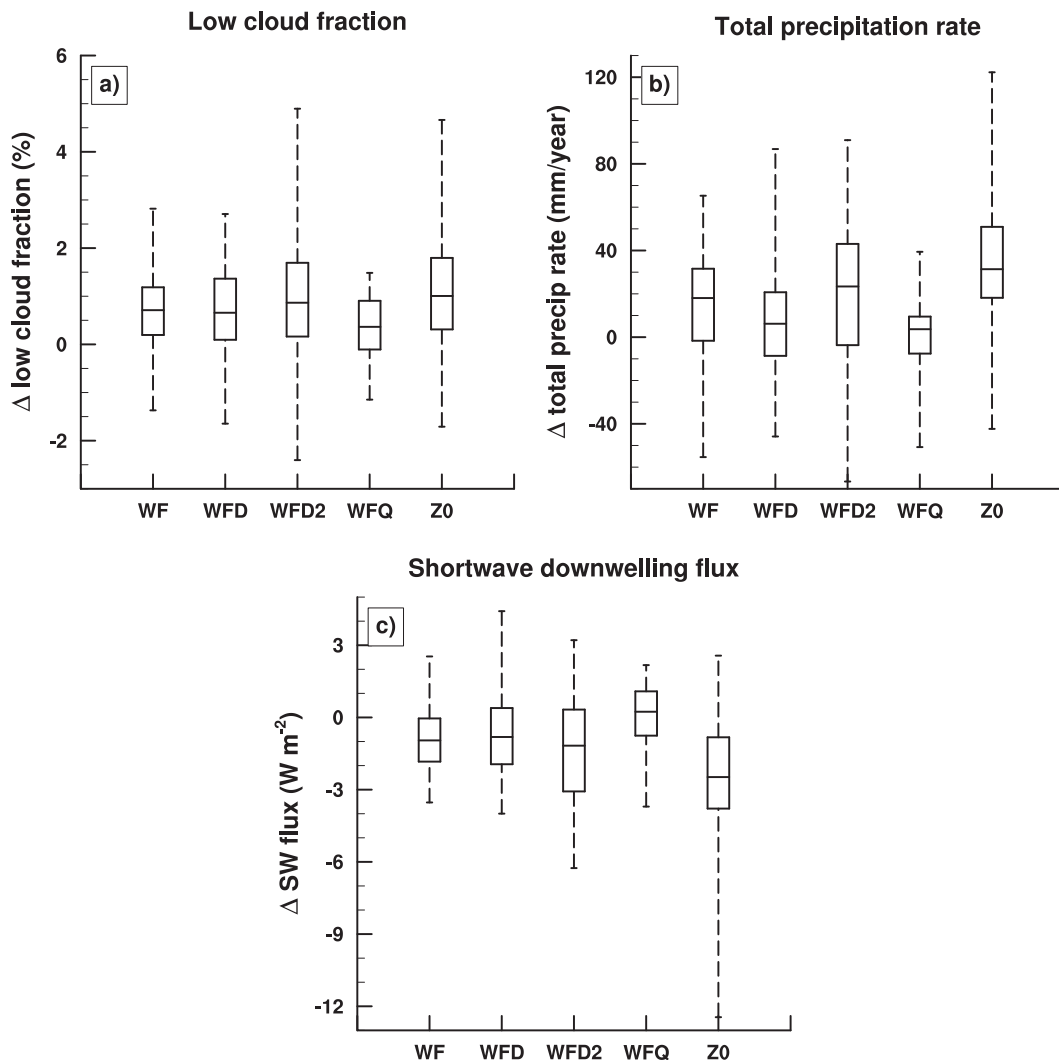## Total precipitation rate

Shortwave downwelling flux

FIG. 9. Box plot of the mean difference over the wind farm areas for a 60-yr period for each case with respect to CTL for (a) low cloud fraction, (b) total precipitation rate, and (c) downwelling shortwave radiation flux. The minimum, first quartile, median, third quartile, and maximum values are indicated.

degree of turning and the reduction in wind speed or the increase in TKE (not shown). Neither is the degree of turning correlated with the latitude of the wind farm (which controls the Coriolis force). However, between the different cases the mean change in wind direction over all the wind farms is found to be correlated with the mean reduction in wind speed (Fig. 10b).

The change in wind direction within the wind farms increases with increasing stable stratification in the lowermost levels (600 m AGL) of the atmosphere (Fig. 10a). In the WF case, the minimum change in wind direction of 1° corresponds with the lowest lapse rate among the wind farms of $2 \, \mathrm{K \, km^{-1}}$. The maximum change in wind direction for this case is 15°. The overall impact on wind direction within the wind farms is shown

in Fig. 10c for the different cases. The mean change in wind direction over all the equal-sized wind farms (excluding the smaller wind farms in the United Kingdom and Germany) is 7° in the WF case. Neglecting turbine blade mixing in WFD reduces the mean change in wind direction very slightly to 6.8°. The WFD2 case shows the greatest change in wind direction of all the cases, where the turbine density is doubled and the greatest wind deficit is seen. The mean change in wind direction is 9.6° in this case. The smallest changes are seen in WFQ, where the wind farms are smaller and the wind deficit is reduced with respect to the other cases. There is a mean change in wind direction of 3.7° in this case. In Z0, where the wind farms are represented as an increase in surface roughness, the mean change in wind direction is 5.9°.
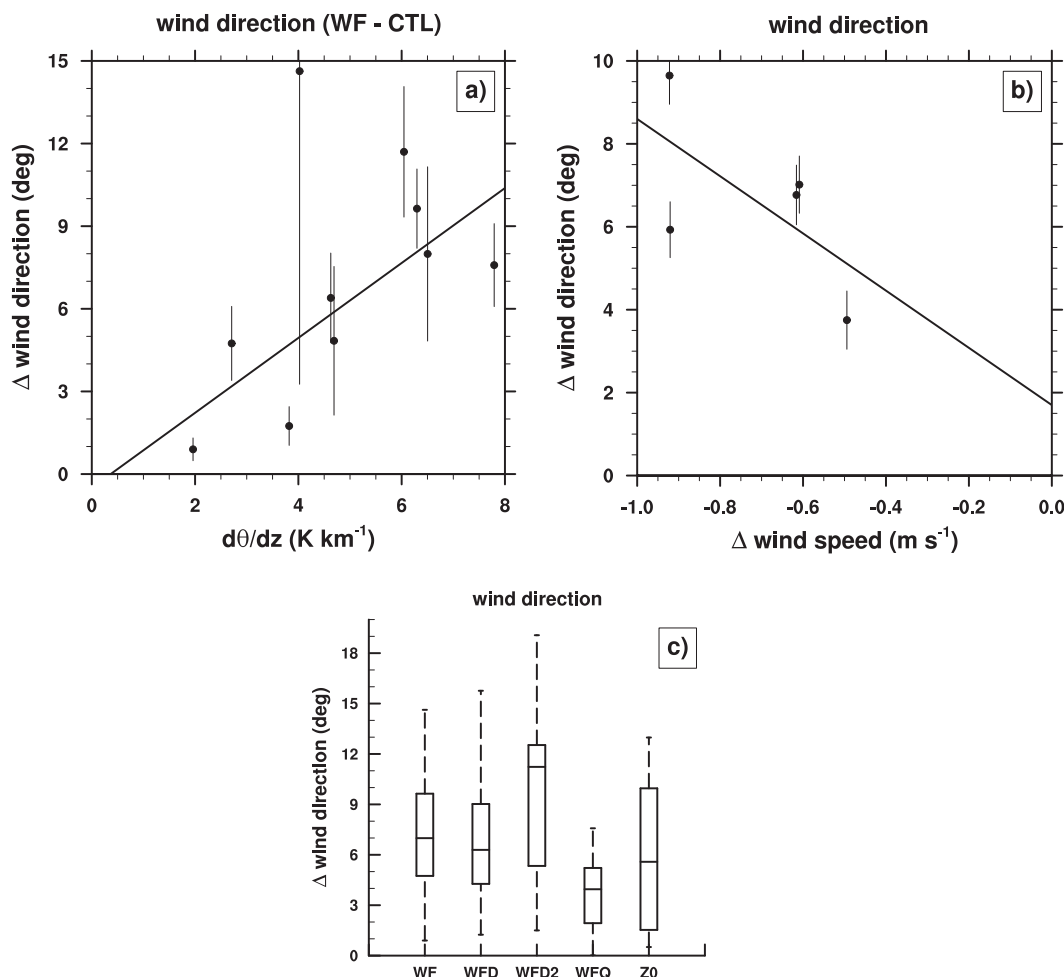
FIG. 10. The mean change in magnitude of wind direction at hub height over the wind farm areas for a 60-yr period with respect to CTL for (a) each wind farm in the WF case as a function of $d\theta/dz$, (b) each case as a function of the mean change in wind speed, and (c) box plot of the change in wind direction for each case. The change in wind direction is negative in the Northern Hemisphere and positive in the Southern Hemisphere. Error bars indicate 95% confidence intervals calculated from annual means (described in section 3b).

Although the wind speed deficit is similar in WFD2 and Z0, the WFD2 case exhibits a greater change in mean wind direction by approximately 60%.

g. Power output

The relatively coarse horizontal resolution does not allow an accurate prediction of the power output of the wind farms, as there are many wind turbines located within a single grid cell, and wake effects on neighboring wind turbines are not represented (within a grid cell). However, the power output is summarized here for completeness. Table 3 shows the mean annual total global power output over a 60-yr period for each of the wind turbine simulations. For the WF simulation, the total power output is 0.981 TW, corresponding to a power output per unit area (over the wind farm areas only) of

0.493 W m^{-2}. The lack of additional turbine mixing in WFD reduces the power output only slightly to 0.979 TW or 0.492 W m^{-2}. The additional TKE to represent turbine mixing was found to have a much greater impact on vertical mixing (reducing the momentum deficit in the wake) in Fitch et al. (2012). The much lower impact here is likely due to the much reduced vertical resolution, as well as the fact that TKE is not a prognosed quantity in the current vertical diffusion scheme.

With a doubling in the number of wind turbines, the greatest power output is seen in the WFD2 case, with a total of 1.259 TW produced (equivalent to 0.633 W m^{-2}). Note that these values are not simply double those of WF—the increased installed turbine density (10 W m^{-2} rather than 5 W m^{-2}) causes greater wake effects on downstream turbines in neighboring grid cells, with less

TABLE 3. Mean annual total power output over a 60-yr period for each wind turbine simulation.

Simulation	Installed capacity (TW)	Installed power density (W m^{-2})	Total wind farm area (10^6 km^2)	Total global power output (TW)	Power output density (W m^{-2})
WF	10	5	2	0.981	0.493
WFD	10	5	2	0.979	0.492
WFD2	20	10	2	1.259	0.633
WFQ	2.5	5	0.5	0.280	0.563

KE available for power generation. The power output in WFD2 is a factor of 1.3 greater than in WF; in other words, 70% of the potential power output has been lost because of increased wake impacts. With reduced wind farm sizes, WFQ generates lower overall power, at 0.280 TW. However, the power output per unit area is increased relative to WF, with 0.563 W m^{-2} generated. The reduced dimensions of the wind farm areas lead to lower wake impacts on downstream KE.

The mean power output over a 60-yr period for one of the most productive wind farms (located in Canada) is shown in Table 4 for the different cases. The power output per unit area for the WF case is 0.789 W m^{-2}, corresponding to a capacity factor (actual power output divided by installed power capacity) of 15.79%. The power output is reduced very slightly in WFD to 0.788 W m^{-2}, a capacity factor of 15.76%. Greatest power output is seen in WFD2, at 1.048 W m^{-2}, although the capacity factor is the lowest of all the cases, at 10.48%, owing to increased wake impacts downstream. With reduced wind farm dimensions and in turn reduced wake effects, WFQ has increased power output relative to WF, at 0.860 W m^{-2}, a capacity factor of 17.21%.

Current operational wind farms exhibit higher power output and capacity factors than those seen in this study. One of the largest wind farms in the United States, Horse Hollow, has an average power output per unit area of 1.55 W m^{-2}, according to Gallman (2011). With an installed capacity of 735 MW over an area of approximately 190 km^2, this gives an average capacity factor of around 40%. The power output per unit area of most large wind farms in the United Kingdom is between 1.5 and 4.5 W m^{-2}, according to MacKay (2013). However, all of the wind farms presently in operation are much smaller than the wind farms simulated here—the

wind farms in WFQ in North America are 38 220 km^2, more than 200 times the size of Horse Hollow wind farm. The wake impacts on downstream turbines are considerably greater in the larger wind farms simulated here, limiting the power output. In addition, the relatively coarse resolution of the model does not resolve finescale features in the topography and atmosphere, which might lead to locally much higher wind speeds and greater power output.

4. Discussion and conclusions

The potential local, regional, and global climate impacts of a large-scale global deployment of wind power have been investigated using a variety of parameterization techniques to represent wind turbines in a global climate model, CAM5. Wind energy is forecasted to provide 15%–18% of the world's electricity demand in 2050, corresponding to an installed capacity of 2.3–2.8 TW (Philibert et al. 2013). This work investigates the potential climate impacts of wind power with installed capacities of 2.5, 10, and 20 TW to provide up to 16%, 65%, and 130%, respectively, of the projected global electricity demand in 2050. The regional and global influences of wind farms on temperature, wind, TKE, cloud, precipitation, and surface heat fluxes are investigated in particular.

Overall impacts on temperature were found to be small, with a mean temperature increase in the lowest model level over a 60-yr period of 0.09 ± 0.07 K over the wind farm areas with a total installed capacity of 10 TW. In this case the wind farms were represented as an elevated momentum sink and source of TKE to represent turbine blade mixing (case WF). The parameterized turbines had a nominal power output of 5 MW and a

TABLE 4. Mean annual power output over a 60-yr period for the wind farm in Canada.

Simulation	Installed power density (W m^{-2})	Wind farm area (km^2)	Power output density (W m^{-2})	Capacity factor (%)
WF	5	152 858	0.789	15.79
WFD	5	152 858	0.788	15.76
WFD2	10	152 858	1.048	10.48
WFQ	5	38 220	0.860	17.21

turbine spacing of 8 rotor diameters. Global-mean temperature impacts were very small, with a slight cooling of no greater than 0.02 K in any of the cases. Doubling the wind turbine density (case WFD2), such that there was a turbine spacing of 4 rotor diameters, to provide a total installed capacity of 20 TW, further increased the mean temperature change over the wind farm areas to $+0.16 \pm 0.09$ K. Decreasing the wind farm areas (case WFQ) to one-quarter that of WF, to provide an installed capacity of 2.5 TW, had similar mean impacts on temperatures within the wind farms as those in the other cases, with a mean increase of 0.12 ± 0.07 K. However, maximum temperature changes were reduced to less than ± 0.4 K. The greatest impact on temperature was seen in the case where the wind farms were instead represented as enhanced surface roughness (case Z0) and to a lesser degree in WFD2. However, in these cases the maximum temperature changes were still less than ± 0.8 K. The temperature changes compare with the observations of Zhou et al. (2012), who found a mean near-surface warming of 0.7 K over a 9-yr period during the night for one season within a large wind farm in Texas. Lower means would be expected over all seasons and for the full diurnal cycle, as temperature changes during the day were found to be small. The maximum warming observed in Smith et al. (2013) and Rajewski et al. (2013) of 1–1.5 K is considerably larger than that seen here, as those observations were from individual nights. In addition, the observations were in the immediate wake of wind turbines, whereas the results presented here are means over a large area. The mean temperature change over two days in the high-resolution simulations of Fitch et al. (2013b) (their WFP case with an identical turbine configuration to the WF case here) was $+0.2$ K, slightly higher than the 60-yr means presented here. The regional modeling study of Vautard et al. (2014), who employed the same wind farm parameterization as in this study, saw a mean warming of 0.1 K over the wind farm areas over a 33-yr period, very similar to the results found here. With the temperature changes reported here, there may be the possibility of some of the diurnal signals during the day and night offsetting each other to produce a smaller mean. However, previous studies (e.g., Zhou et al. 2012; Smith et al. 2013; Fitch et al. 2013b) have found the cooling signal during the day in an unstable boundary layer is much weaker than the warming signal at night with a stable boundary layer. With neutral boundary layers there are no changes in temperature.

Outside the wind farm areas, impacts on temperature were generally slight, especially in WFQ, but increased in WFD2 and Z0. In Z0, the increased roughness length for momentum over the wind farm areas was responsible for reducing the resistance to heat transfer between the land and atmosphere, thus increasing the sensible heat fluxes and near-surface temperatures over some of the wind farm areas. The maximum temperature increase of 0.7 K in Z0 is lower than the 1-K warming seen in Fitch et al. (2013b) (for their Z0_ZIL case, which most closely follows the configuration here)—a 60-yr mean would be expected to show lower extremes than the 2-day diurnal cycle in their study. In addition, the extra resistances to heat transfer for vegetated surfaces apply [Eqs. (17) and (18)] in the land surface model employed here, whereas Fitch et al. (2013b) used idealized surface boundary conditions. A greater warming of 1 K was also seen over the wind farm areas in Keith et al. (2004, their Fig. 5a). In their study, they increased the roughness lengths for momentum and heat by the same amount, which was shown in Fitch et al. (2013b) to produce the largest increase in surface heat fluxes and near-surface temperatures. In the present study only the roughness length for momentum is directly modified. The roughness length for momentum was also nearly a factor of 2 greater in their study. In addition, the displacement height was not changed. The reduction in displacement height here further increased the resistance to heat transfer and in turn the surface heat fluxes. Greater climate impacts were found by Miller et al. (2011), who found maximum changes close to those projected with a doubling in carbon dioxide. In a similar fashion to Keith et al. (2004), they modeled wind turbines as an increase in surface drag.

Influences on wind speed were mostly confined to the wind farm areas and immediate surroundings. Wake effects became more substantial in WFD2 with a doubling in wind turbine density. The WF case showed a mean reduction in the wind speed over the wind farm areas of $0.6\,\mathrm{m\,s^{-1}}$ ($19\% \pm 1.4\%$) at hub height (100 m AGL) over a 60-yr period, which increased to $0.9\,\mathrm{m\,s^{-1}}$ ($29\% \pm 1.2\%$) in WFD2. The largest decrease in the wind speed was seen in the Z0 case, with wake effects exaggerated compared to WF. Although the roughness length chosen was appropriate for the wind turbine size and spacing used in WF (according to LES analysis by Calaf et al. 2011), the results presented here suggest it is more appropriate for a doubling in turbine density, as the reductions in wind speed follow the WFD2 case more closely. The mean reduction in wind speed within the wind farm areas is $0.9\,\mathrm{m\,s^{-1}}$ in the Z0 case, corresponding to a reduction of $29\% \pm 1.2\%$. The wind speed deficits seen in WF compare well with those in Fitch et al. (2013a), who found maximum deficits of 10% and 30% during the day and night, respectively. The mean reduction of 19% in the WF case here falls between these values. Global-mean changes in wind speed were very slight in all cases with a reduction of no greater than 0.7%.

In addition to impacting the wind speed, the wind farms were also found to influence the wind direction within the wind farms and the immediate surroundings. Wind farms act to increase the turbulent drag, in turn increasing the velocity component directed toward lower pressure. As a result, the wind farms caused the wind to turn to the left of the geostrophic wind in the Northern Hemisphere and to the right in the Southern Hemisphere. The degree of turning was found to be dependent on the stability in the lowermost levels of the atmosphere, with increased turning in more stable layers. In the WF case, the wind direction changed by $\pm 7° \pm 0.7°$ on average at hub height, which increased to $\pm 9.6° \pm 0.7°$ in WFD2. With smaller wind farms in WFQ, the mean change in wind direction was reduced to $\pm 3.7° \pm 0.7°$. A similar degree of turning above the rotor area was found in Fitch et al. (2013a), who saw a 4° backing in the wind in their Northern Hemisphere simulation.

The modeled wind farms generate TKE by increasing the wind shear above the rotor area and also directly increase TKE within the rotor area to represent turbine blade mixing (in the WF, WFD2, and WFQ cases only). TKE was found to change within the wind farm areas only, with a $17\% \pm 0.8\%$ increase on average at hub height in WF. However, without representation of turbine blade mixing in WFD, the TKE was reduced by $6\% \pm 0.7\%$ relative to the control case and by 23% relative to WF. The reduced TKE very slightly increased the momentum deficit within the wind farms. The impact of TKE on momentum deficits was found to be more important in the study by Fitch et al. (2012), most likely because of the much higher vertical resolution. A doubling in turbine density (WFD2) increased the TKE by 30% relative to the control case. Greatest TKE was seen in Z0, where the TKE was increased by $56\% \pm 0.8\%$ at hub height. In this case TKE increased the most near the surface, where enhanced surface roughness led to large shear production of TKE.

Impacts on sensible and latent heat fluxes were small, with changes in all cases apart from Z0 less than $\pm 1.5\%$ over the wind farm areas. Outside the wind farm areas, there was little significant change in sensible and latent heat fluxes. The small change in surface heat fluxes in the WF cases agree well with the observations of Rajewski et al. (2013), who saw little change. These results are also consistent with the wind tunnel experiments of Zhang et al. (2013), who observed overall mean reductions in the sensible heat flux between 0% and 4%.

The low cloud amount was found to increase slightly over the wind farm areas in all cases, with a mean increase of $0.7\% \pm 0.3\%$ in the WF case. Flow convergence and uplift at the wind farms was responsible, with greater momentum deficits in the WFD2 and Z0 cases

generating increased uplift and low cloud amounts, with a mean increase of $1\% \pm 0.3\%$ in these cases. The slight increase in low cloud led to small increases in precipitation over the wind farm areas, with a mean increase of $2.6\% \pm 1.5\%$ in the WF case, which increased to $3.4\% \pm 1.6\%$ and $6\% \pm 1.7\%$ in the WFD2 and Z0 cases, respectively. Global-mean changes in low cloud and precipitation were very slight. A 1% increase in precipitation was seen in the regional climate simulation of Fiedler and Bukovsky (2011) in a region surrounding a large wind farm. The mean increase in precipitation in Vautard et al. (2014), who found an increase of $0.01 \, \mathrm{mm \, day^{-1}}$, is similar to the WFQ case here.

Overall, we find negligible climate impacts resulting from a global deployment of large-scale wind farms in regionally high densities over land for a total installed capacity of 2.5 TW. Changes in temperature, cloud, precipitation, and sensible and latent heat fluxes were slight. Impacts on wind speed and TKE were more significant but mostly confined to the wind farm areas only. Increasing the wind farm areas for a total capacity of 10 TW increased impacts, but only marginally, and they were still mostly confined to the wind farm areas only. A doubling in turbine density for a turbine spacing of 4 rotor diameters and a total installed capacity of 20 TW again increased impacts slightly, but changes in temperature remained small overall. However, wind speed deficits became more noticeable in the wind farm areas and immediate surroundings. Representing wind farms instead with an increase in surface roughness was found to give similar mean values as the elevated momentum sink approach (WF), with similar mean temperature changes. However, maximum changes increased significantly, and wind speed deficits and TKE were increased by 50% and by a factor of 3, respectively. Relative to WF, the increase in precipitation was more than a factor of 2 greater, and surface heat fluxes were also exaggerated. Although using the Zilitinkevich (1995) formulation for the roughness length for heat and a displacement height of zero improves upon previous results using the enhanced surface roughness approach for representing wind farms, there are still considerable deficiencies. The vertical profiles of wind speed and TKE are very different from the elevated approach, with greatest wind deficits near the surface rather than at rotor height. Greatest TKE production was also seen near the ground. Neglecting turbine blade mixing (an enhancement of the TKE within the rotor area) has a small impact, with very slightly greater wind speed deficits. However, the vertical profile of TKE is unrealistic, with reductions in TKE within the rotor area relative to the control case, owing to a reduction in the wind shear. The impact of enhanced TKE within the rotor area is expected to be more important

with higher vertical resolution and may be sensitive to the vertical diffusion scheme.

The present study did not employ a coupled ocean model, and instead SSTs followed climatological means. Given that the wind farm impacts are mostly limited to the wind farm areas themselves, it is unlikely that a coupled ocean model would change the results significantly. However, for offshore wind farms, a coupled ocean model would be more relevant and will be explored in future.

The elevated momentum sink parameterization was found to perform well with coarser vertical resolution, with little sensitivity to vertical resolution seen when there were at least two model levels within the rotor area (Fitch et al. 2012). In these simulations, two model levels intersect the rotor area. Fitch et al. (2013b) also tested the parameterization with a vertical resolution typical in global climate models and found it compared well with higher resolution simulations. With the coarse horizontal resolution typical of global climate models, there are many wind turbines located within a single grid cell, and wake effects on neighboring wind turbines are not represented. However, the wake of groups of turbines within a grid cell may impact turbines in a neighboring cell. This approach cannot be used to give accurate estimates of turbine power output, though overall mean impacts on the atmosphere are reasonably represented, with results consistent with the few observations available. The results presented here are average impacts over a large area. In the immediate wake of turbines, impacts are expected to be greater (Rajewski et al. 2013; Smith et al. 2013). A maximum power output per unit area of around $1\,\mathrm{W\,m}^{-2}$ was seen over the wind farm areas for the WFD2 case, which agrees well with Adams and Keith (2013). However, greater turbine densities were not tested to see if this value increased.

The results presented here are indicative of the maximum mean wind farm impacts likely to be seen. Wind farm areas are unlikely to exceed those simulated here for the foreseeable future. In addition, the mean wind climatology for all the wind farms is in the range where the turbine thrust coefficient is a maximum, resulting in the greatest fraction of KE extracted from the flow and the largest enhancement in TKE. Marvel et al. (2013) found a slight mean warming of 0.1 K in simulations of wind turbines uniformly covering the entire globe over land. The results presented here show that wind farm impacts increase as turbine density increases and that, in order to minimize their effects on the atmosphere, wind turbines should be less densely spaced. The eight-rotor-diameter spacing examined here in the 2.5 and 10 TW capacities is typical of large wind turbine configurations. Overall, wind farm impacts are much weaker than those expected from greenhouse gas emissions (IPCC 2013).

REFERENCES

Adams, A. S., and D. W. Keith, 2013: Are global wind power resource estimates overstated? *Environ. Res. Lett.,* **8,** 015021, doi:10.1088/1748-9326/8/1/015021.

Baidya Roy, S., and J. J. Traiteur, 2010: Impacts of wind farms on surface air temperatures. *Proc. Natl. Acad. Sci. USA,* **107,** 17 899–17 904, doi:10.1073/pnas.1000493107.

——, S. W. Pacala, and R. L. Walko, 2004: Can large wind farms affect local meteorology? *J. Geophys. Res.,* **109,** D19101, doi:10.1029/2004JD004763.

Barrie, D. B., and D. B. Kirk-Davidoff, 2010: Weather response to a large wind turbine array. *Atmos. Chem. Phys.,* **10,** 769–775, doi:10.5194/acp-10-769-2010.

Bretherton, C. S., and S. Park, 2009: A new moist turbulence parameterization in the Community Atmosphere Model. *J. Climate,* **22,** 3422–3448, doi:10.1175/2008JCLI2556.1.

Calaf, M., M. B. Parlange, and C. Meneveau, 2011: Large eddy simulation study of scalar transport in fully developed wind-turbine array boundary layers. *Phys. Fluids,* **23,** 126603, doi:10.1063/1.3663376.

Fiedler, B. H., and M. S. Bukovsky, 2011: The effect of a giant wind farm on precipitation in a regional climate model. *Environ. Res. Lett.,* **6,** 045101, doi:10.1088/1748-9326/6/4/045101.

Fitch, A. C., J. B. Olson, J. K. Lundquist, J. Dudhia, A. K. Gupta, J. Michalakes, and I. Barstad, 2012: Local and mesoscale impacts of wind farms as parameterized in a mesoscale NWP model. *Mon. Wea. Rev.,* **140,** 3017–3038, doi:10.1175/MWR-D-11-00352.1.

——, J. K. Lundquist, and J. B. Olson, 2013a: Mesoscale influences of wind farms throughout a diurnal cycle. *Mon. Wea. Rev.,* **141,** 2173–2198, doi:10.1175/MWR-D-12-00185.1.

——, J. B. Olson, and J. K. Lundquist, 2013b: Parameterization of wind farms in climate models. *J. Climate,* **26,** 6439–6458, doi:10.1175/JCLI-D-12-00376.1.

Gallman, P. G., 2011: *Green Alternatives and National Energy Strategy: The Facts behind the Headlines.* Johns Hopkins University Press, 208 pp.

Global Wind Energy Council, 2014: Global wind statistics 2013. Global Wind Energy Council Rep., 4 pp. [Available online at http://www.gwec.net/wp-content/uploads/2014/02/GWEC-PRstats-2013_EN.pdf.]

Holton, J. R., 2004: *An Introduction to Dynamic Meteorology.* Elsevier Academic Press, 535 pp.

IPCC, 2013: Summary for policymakers. *Climate Change 2013: The Physical Science Basis,* T. F. Stocker et al., Eds., Cambridge University Press, 1–29.

Ivanova, L. A., and E. D. Nadyozhina, 2000: Numerical simulation of wind farm influence on wind flow. *Wind Eng.,* **24,** 257–269, doi:10.1260/0309524001495620.

Jacobson, M. Z., and C. L. Archer, 2012: Saturation wind power potential and its implications for wind energy. *Proc. Natl. Acad. Sci. USA,* **109,** 15 679–15 684, doi:10.1073/pnas.1208993109.

Keith, D., J. DeCarolis, D. Denkenberger, D. Lenschow, S. Malyshev, S. Pacala, and P. J. Rasch, 2004: The influence of large-scale

wind power on global climate. *Proc. Natl. Acad. Sci. USA,* **101,** 16 115–16 120, doi:10.1073/pnas.0406930101.

Kirk-Davidoff, D. B., and D. W. Keith, 2008: On the climate impact of surface roughness anomalies. *J. Atmos. Sci.,* **65,** 2215–2234, doi:10.1175/2007JAS2509.1.

Lindvall, J., G. Svensson, and C. Hannay, 2013: Evaluation of near-surface parameters in the two versions of the atmospheric model in CESM1 using flux station observations. *J. Climate,* **26,** 26–44, doi:10.1175/JCLI-D-12-00020.1.

Lu, H., and F. Porté-Agel, 2011: Large-eddy simulation of a very large wind farm in a stable atmospheric boundary layer. *Phys. Fluids,* **23,** 065101, doi:10.1063/1.3589857.

MacKay, D., 2013: Could energy-intensive industries be powered by carbon-free electricity? *Philos. Trans. Roy. Soc. London,* **371A,** 20110560, doi:10.1098/rsta.2011.0560.

Marvel, K., B. Kravitz, and K. Caldeira, 2013: Geophysical limits to global wind power. *Nat. Climate Change,* **3,** 118–121, doi:10.1038/nclimate1683.

Mellor, G. L., and T. Yamada, 1982: Development of a turbulence closure model for geophysical fluid problems. *Rev. Geophys.,* **20,** 851–875, doi:10.1029/RG020i004p00851.

Miller, L. M., F. Gans, and A. Kleidon, 2011: Estimating maximum global land surface wind power extractability and associated climatic consequences. *Earth Syst. Dyn.,* **2,** 1–12, doi:10.5194/esd-2-1-2011.

Neale, R. B., and Coauthors, 2012: Description of the NCAR Community Atmosphere Model (CAM 5.0). NCAR Tech. Note NCAR/TN-486+STR, 268 pp. [Available online at http://www.cesm.ucar.edu/models/cesm1.0/cam/docs/description/cam5_desc.pdf.]

Oleson, K. W., and Coauthors, 2010: Technical description of version 4.0 of the Community Land Model (CLM). NCAR Tech. Note NCAR/TN-478+STR, 257 pp. [Available online at http://www.cesm.ucar.edu/models/ccsm4.0/clm/CLM4_Tech_Note.pdf.]

Philibert, C., and Coauthors, 2013: Technology roadmap: Wind energy, 2013 edition. OECD/IEA Rep., 63 pp. [Available online at https://www.iea.org/publications/freepublications/publication/Wind_2013_Roadmap.pdf.]

Rajewski, D. A., and Coauthors, 2013: Crop Wind Energy Experiment (CWEX): Observations of surface-layer, boundary layer, and mesoscale interactions with a wind farm. *Bull. Amer. Meteor. Soc.,* **94,** 655–672, doi:10.1175/BAMS-D-11-00240.1.

REpower, 2014: REpower 5M turbine. [Available online at http://www.renugen.co.uk/content/large_wind_turbine_brochures/large_wind_turbine_brochures/repower_5m.pdf.]

Smith, C. M., R. J. Barthelmie, and S. C. Pryor, 2013: *In situ* observations of the influence of a large onshore wind farm on near-surface temperature, turbulence intensity and wind speed profiles. *Environ. Res. Lett.,* **8,** 034006, doi:10.1088/1748-9326/8/3/034006.

Vautard, R., F. Thais, I. Tobin, F. M. Bréon, J. G. D. de Lavergne, A. Colette, P. Yiou, and P. M. Ruti, 2014: Regional climate model simulations indicate limited climatic impacts by operational and planned European wind farms. *Nat. Commun.,* **5,** 3196, doi:10.1038/ncomms4196.

Wang, C., and R. G. Prinn, 2010: Potential climatic impacts and reliability of very large-scale wind farms. *Atmos. Chem. Phys.,* **10,** 2053–2061, doi:10.5194/acp-10-2053-2010.

——, and ——, 2011: Potential climatic impacts and reliability of large-scale offshore wind farms. *Environ. Res. Lett.,* **6,** 025101, doi:10.1088/1748-9326/6/2/025101.

Zhang, W., C. D. Markfort, and F. Porté-Agel, 2013: Experimental study of the impact of large-scale wind farms on land–atmosphere exchanges. *Environ. Res. Lett.,* **8,** 015002, doi:10.1088/1748-9326/8/1/015002.

Zhou, L., Y. Tian, S. Baidya Roy, C. Thorncroft, L. F. Bosart, and Y. Hu, 2012: Impacts of wind farms on land surface temperature. *Nat. Climate Change,* **2,** 539–543, doi:10.1038/nclimate1505.

Zilitinkevich, S. S., 1995: Non-local turbulent transport pollution dispersion aspects of coherent structure of convective flows. *Air Pollution III: Volume I. Air Pollution Theory and Simulation,* H. Power et al., Eds., Computational Mechanics Publications, 53–60.